Ocean Engineering 343 (2026) 123418

Contents lists available at ScienceDirect

Ocean Engineering

journal homepage: www.elsevier.com/locate/oceaneng

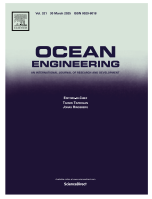

Research paper

A computational method for the fluid-structure interaction in nonlinear ocean waves using the nonlinear Schrödinger equation

Marten Hollm [a,*], Robert Seifried [a]

[a] Institute of Mechanics and Ocean Engineering, Hamburg University of Technology, Eissendorfer Strasse 42, Hamburg, 21073, Germany

ARTICLE INFO

Keywords:
Nonlinear Schrödinger equation
Computational method
Fluid-structure interaction
Ocean waves
Irregular sea

ABSTRACT

An efficient computation of the fluid-structure interaction (FSI) between mechanical structures and ocean waves is an important topic for many applications in ocean engineering and naval architecture. For many of such applications, it is often sufficient to consider the FSI within the potential flow theory instead of using the Navier-Stokes equations. However, the numerical solution of the governing equations of the potential flow theory is still computationally expensive. This work contributes to the improvement of the currently available numerical schemes, which compute the FSI in nonlinear ocean waves. The approach used in this work is based on the nonlinear Schrödinger equation (NLS). Compared to the governing equations of potential flow theory, solutions of the NLS can be computed much more efficiently. This efficiency advantage is used to develop a method that allows a fast computation of the FSI in nonlinear water waves.

The developed method is investigated with regard to its accuracy, application areas, and computational effort. Here, numerical results for the hydrodynamic forces acting on mechanical structures and the resulting motion of the structures are analyzed. It is found that the NLS offers an interesting possibility to efficiently investigate the behavior of structures excited by nonlinear ocean waves.

1. Introduction

Ships and offshore structures in the ocean differ widely in their geometric shape and submerged depth. When designing these structures, appropriate safety limits must be considered. This can be done by knowing the hydrodynamic loads acting on the different mechanical structures. However, not only the hydrodynamic loads, but also the system response of the mechanical structures to the ocean waves can be of interest for many applications. Here, the fluid-structure interaction (FSI) between the different mechanical structures and the incoming water waves must be analyzed. Since real ocean seas are nonlinear, an efficient analysis of the FSI between mechanical structures and nonlinear water waves is of great practical interest in many application areas.

In general, the behavior of fluids can be modeled using the Navier-Stokes equations. Various free and commercial codes are available to calculate herewith the FSI with moving structures. Many codes, like OpenFOAM, REEF3D, and STAR-CCM+ solve the fully nonlinear Navier-Stokes equations with the inclusion of appropriate turbulence closure models. In theory, this set of equations can handle very complex phenomena with almost no limitations (Lin, 2008). However, solving this set of equations requires a large computational effort, often requiring high-performance computer facilities and well-trained staff (Greaves and Iglesias, 2018). This is a particular problem with stochastic sea states, as many simulations with long simulation times are required to describe the dynamics of a structure in random waves representatively.

However, for many applications, it is often sufficient to consider the FSI within the potential flow theory (Lin, 2008; Greaves and Iglesias, 2018). Models using potential flow theory are the second most capable of simulating complex flows after those based on the Navier-Stokes equations (Greaves and Iglesias, 2018). They can be used to model the behavior of homogeneous, incompressible, non-viscous, and irrotational fluids, where surface tension effects are neglected. The nonlinear governing equations of potential flow theory can be solved, for example, using the Quasi Arbitrary Lagrangian-Eulerian Finite Element Method, which was first developed by Ma and Yan (2006). However, since they involve nonlinear boundary conditions at the unknown free water sea surface, solving the fully nonlinear equations of fluid motion takes too much computation time to be heavily applied in the design of offshore structures (Shao et al., 2022). Therefore, the nonlinear governing equations of potential flow theory are simplified in many ocean engineering applications by applying Stokes perturbation expansion or Taylor series expansions, see e.g. (Mei, 1983; Malenica and Molin, 1995). If only the corresponding first-order terms of the Taylor series expansions

* Corresponding author.
E-mail addresses: marten.hollm@tuhh.de (M. Hollm), robert.seifried@tuhh.de (R. Seifried).

https://doi.org/10.1016/j.oceaneng.2025.123418
Received 20 August 2025; Received in revised form 6 October 2025; Accepted 1 November 2025
Available online 15 November 2025

are taken into account, linearized equations can be obtained. The corresponding linearized wave theory can be used to model the dynamics of water waves with small wave heights H and low wave velocities very well (Newman, 2018). However, a nonlinear wave theory must be used to accurately model the behavior of larger and faster waves. Corresponding nonlinear wave theories can be derived by considering additional higher-order terms in the Taylor series expansions of the nonlinear governing equations, see e.g. (Malenica and Molin, 1995; Hollm and Seifried, 2023).

Considering the computational effort, it has to be noted that simulations using potential flow theory are faster than those using the Navier-Stokes equations in combination with an appropriate turbulence closure model. However, their computational costs are still high (Lin, 2008; Greaves and Iglesias, 2018). Even for the case that the nonlinear governing equations of potential flow theory are simplified applying the Taylor series expansions mentioned above, the calculation of the FSI in realistic nonlinear water waves still requires long computation times. This is because wave-wave interactions must be considered to describe random nonlinear water waves, which can be very time-consuming (Slunyaev et al., 2014).

However, there are other ways to describe nonlinear water waves. One is offered by using the nonlinear Schrödinger equation (NLS), which is a partial differential equation for the wave envelope ψ of the water waves. The NLS can be used to accurately model nonlinear water waves in deep water with a narrow spectral bandwidth and moderate wave steepness, see e.g. (Dysthe, 1979; Witt, 2019; Osborne, 2010). Starting from the wave envelope ψ of nonlinear water waves, Carter et al. (2020) derived a general representation for the corresponding velocity potential. This velocity potential is needed for calculating the hydrodynamic forces and the associated motion of floating structures in nonlinear water waves. Since the theory of Carter et al. (2020) is very new, it has not yet been used to calculate the FSI between mechanical structures and nonlinear water waves. In this paper, the theory of Carter et al. (2020) is used to compute this FSI in nonlinear water waves.

Compared to the nonlinear governing equation of the potential flow theory, the NLS has several advantages. For example, a variety of analytical solutions of the NLS have been presented, see e.g. (Peregrine, 1983; Osborne, 2010; Chabchoub, 2013; Slunyaev et al., 2013; Carter et al., 2020) and the references therein. Furthermore, it has been found that the NLS can describe many features of the dynamics of rogue waves, which are found to arise as a result of nonlinear self-focusing phenomena (Onorato et al., 2001). Moreover, it has been conjectured in different studies that specific solutions of the NLS are prototypes of rogue ocean waves, see e.g. (Dysthe and Trulsen, 1999; Shrira and Geogjaev, 2010; Dostal et al., 2020). In addition, numerical solutions of the NLS can be computed much more efficiently than solutions of the nonlinear governing equation of the potential flow theory. Finally, irregular sea states can be efficiently generated with the NLS by applying the approach presented in (Hollm et al., 2021, 2022a). All these advantages make it interesting to use also the NLS to compute the FSI between structures and nonlinear water waves, which has not been done before.

The aim of this work is to establish a computational method that can be used to calculate the nonlinear FSI between a mechanical structure and nonlinear water waves efficiently. The corresponding approach is based on the NLS. Compared to the nonlinear governing equations of potential flow theory, solutions of the NLS can be computed much more efficiently. In this work, this efficiency is used to develop a method that allows a fast computation of the FSI between a mechanical structure and nonlinear water waves. The developed method is investigated with regard to its application areas, accuracy, and computational effort. The computational method presented and analyzed in this work is based on (Hollm, 2025).

In this work, the NLS is used for the first time to numerically compute the FSI. Here, the application focuses on problems in the field of ocean engineering. The advantages of the NLS, which are mentioned above, are used to develop a novel computational framework that significantly enhances the efficiency of simulating nonlinear FSI problems. As the results of the FSI depend on the geometry of the corresponding structure interacting with the water, the FSI can only be computed numerically for structures of general geometry. This work introduces an innovative application of the NLS to the field of FSI, which establishes a novel pathway for research in this area.

It has to be noted that the NLS in standard form cannot be used to model general nonlinear water waves, but only those in deep water with a narrow spectral bandwidth and moderate wave steepness. However, several extended versions of the NLS exist, which can model water waves with a larger wave steepness and broader spectral bandwidth than the NLS in standard form, or are not restricted to deep water. These extended versions can be found, for example, in (Mei, 1983; Dysthe, 1979; Trulsen and Dysthe, 1996; Toffoli et al., 2010; Adcock and Taylor, 2016). While the present work does not consider these extended versions of the NLS, it provides an initial overview of the advantages and limitations of using the NLS framework to compute the FSI with nonlinear water waves.

The work is organized as follows: First, all fundamental equations to model the FSI between ocean waves and floating mechanical systems are introduced in Section 2. After introducing the NLS in Section 3, it is presented in Section 4 how the NLS can be used to compute the FSI between a structure and nonlinear water waves. The accuracy of the proposed computational method is also analyzed here. In Section 5, a finite difference method is presented to compute the FSI between incoming nonlinear water waves and a given mechanical structure numerically. In Section 6, the introduced finite difference scheme is validated. Afterward, the developed computational method and numerical scheme are used in Section 7 to simulate the FSI between a cylindrical floating body and nonlinear water waves utilizing the NLS. Analyzing the corresponding results, the application areas and computational effort of the developed scheme are investigated. Finally, this work ends with a conclusion in Section 8.

2. Modeling of water waves

In this section, all fundamental equations to model the FSI between ocean waves and floating mechanical structures are reviewed, which are necessary for the later developed computational method.

2.1. Fully nonlinear equations of fluid motion

The behavior of homogeneous, incompressible, non-viscous, irrotational fluids, where surface tensions are neglected, is considered. Let t denote the time and C: $\{O, x, y, z\}$ be a Cartesian coordinate system, whereby $z = 0$ describes the plane of the undisturbed free sea surface and the z-axis is positive upwards. The vertical displacement of any point on the free sea surface is defined by the function $z = \eta = \eta(x, y, t)$. Here, it is assumed that the water waves are not breaking such that the value of $\eta(x, y, t)$ is uniquely defined everywhere.

Using the assumptions mentioned above, the fluid motion can be described by the velocity potential $\phi = \phi(x, y, z, t)$. The governing equations of fluid motion of potential flow theory result in

$$\nabla^2\phi = \phi_{xx} + \phi_{yy} + \phi_{zz} = 0, \qquad \text{for} \quad -h \le z \le \eta(x, y, t), \tag{1a}$$

$$\eta_t + \phi_x\eta_x + \phi_y\eta_y = \phi_z, \qquad \text{for} \quad z = \eta(x, y, t), \tag{1b}$$

$$\phi_t + \frac{1}{2}\nabla\phi \cdot \nabla\phi + g\eta = 0, \qquad \text{for} \quad z = \eta(x, y, t), \tag{1c}$$

$$\phi_z = 0, \qquad \text{for} \quad z = -h, \tag{1d}$$

see e.g. (Newman, 2018). Here, ∇ denotes the nabla operator in space, g is the gravitational constant, and h is the constant water depth with a rigid, impermeable plane. It has to be noted that the external pressure exerted on the sea surface η is assumed to be zero.

By solving Eq. (1), the dynamics of water waves on the open sea can be calculated. However, if there are additional boundaries such as the surface of walls or mechanical structures, additional boundary conditions (BCs) must be formulated here. In this work, general floating bodies are considered, which are impermeable to water. Let S_B be the wetted surface of the mechanical structure and $\mathbf{u}$ the velocity of a point on S_B. Then the BC at S_B is given by

$$\nabla\phi\cdot\mathbf{n}=\mathbf{u}\cdot\mathbf{n},\quad \text{at } (x,y,z)\in S_\mathrm{B}, \tag{2}$$

whereby $\mathbf{n}$ denotes the normal vector at S_B pointing out of the fluid and hence into the body.

2.2. Approximation of governing equations

Solving the fully nonlinear equations from Eq. (1) is computationally expensive. This section introduces wave theories that approximate Eq. (1). Since the nonlinearity of Eq. (1) comes from the BCs (1b) and (1c), this section focuses on a suitable approximation of these equations.

The first step is to combine the two BCs (1b) and (1c) into a single BC. This is done by considering the substantial derivative of the BC (1c) and eliminating the term η_t in the resulting expression using BC (1b), see (Newman, 2018). The resulting combined BC is exact and depends only on the velocity potential ϕ, except that it has to be applied at the unknown sea surface $z=\eta$. In the next step, the combined BC is expanded from $z=\eta(x,y,t)$ to $z=0$ using Taylor series expansions. Considering all terms up to order $O(\phi^4)$, the resulting BC at $z=0$ is given by

$$\begin{aligned}&\phi_{tt}+g\phi_z+2\nabla\phi\cdot\nabla\phi_t+\frac{1}{2}\nabla\phi\cdot\nabla(\nabla\phi\cdot\nabla\phi)\\&-\frac{1}{g}\phi_t\frac{\partial}{\partial z}\left(\phi_{tt}+g\phi_z+2\nabla\phi\cdot\nabla\phi_t\right)\\&-\frac{1}{g}\left(-\frac{1}{g}\phi_t\phi_{tz}+\frac{1}{2}\nabla\phi\cdot\nabla\phi\right)\frac{\partial}{\partial z}\left(\phi_{tt}+g\phi_z\right)\\&+\frac{1}{2g^2}\left(\phi_t\right)^2\frac{\partial^2}{\partial z^2}\left(\phi_{tt}+g\phi_z\right)=0+O(\phi^4),\end{aligned} \tag{3}$$

see e.g. (Newman, 2018) for details.

Next, the nonlinear BC (3) is approximated by a sequence of linear equations. Here, it is assumed that ϕ, η, and the velocity vector $\mathbf{u}$ of a point on S_B can be expressed by perturbation series of the form

$$\phi=\varepsilon\phi^{(1)}+\varepsilon^2\phi^{(2)}+\varepsilon^3\phi^{(3)}+O(\varepsilon^4), \tag{4a}$$

$$\eta=\varepsilon\eta^{(1)}+\varepsilon^2\eta^{(2)}+\varepsilon^3\eta^{(3)}+O(\varepsilon^4), \tag{4b}$$

$$\mathbf{u}=\varepsilon\mathbf{u}^{(1)}+\varepsilon^2\mathbf{u}^{(2)}+\varepsilon^3\mathbf{u}^{(3)}+O(\varepsilon^4), \tag{4c}$$

see e.g. (Malenica and Molin, 1995). Here, ε is a small perturbation parameter related to the wave steepness kA with wavenumber k and wave amplitude A. Based on the pioneering work of Stokes (Stokes, 1847), who used this approach to find periodic solutions of nonlinear water waves, these perturbation series are known as Stokes' expansions. Substituting Eq. (4a) into Eq. (3) and sorting by the resulting exponents in ε^i yields

$$\begin{aligned}&\varepsilon\left(\phi_{tt}^{(1)}+g\phi_z^{(1)}\right)+\varepsilon^2\left(\phi_{tt}^{(2)}+g\phi_z^{(2)}-F^{(2)}(\phi^{(1)})\right)\\&\qquad+\varepsilon^3\left(\phi_{tt}^{(3)}+g\phi_z^{(3)}-F^{(3)}(\phi^{(1)},\phi^{(2)})\right)=0+O(\varepsilon^4).\end{aligned} \tag{5}$$

Here, the functions $F^{(2)}$ and $F^{(3)}$ are defined as

$$F^{(2)}(\phi^{(1)}):=-2\nabla\phi^{(1)}\cdot\nabla\phi_t^{(1)}+\frac{1}{g}\phi_t^{(1)}\frac{\partial}{\partial z}\left(\phi_{tt}^{(1)}+g\phi_z^{(1)}\right), \tag{6}$$

$$\begin{aligned}F^{(3)}(\phi^{(1)},\phi^{(2)}):=&-2\nabla\phi^{(1)}\cdot\nabla\phi_t^{(2)}-2\nabla\phi^{(2)}\cdot\nabla\phi_t^{(1)}\\&-\frac{1}{2}\nabla\phi^{(1)}\cdot\nabla\left(\nabla\phi^{(1)}\cdot\nabla\phi^{(1)}\right)+\frac{1}{g}\phi_t^{(2)}\frac{\partial}{\partial z}\left(\phi_{tt}^{(1)}+g\phi_z^{(1)}\right)\\&+\frac{1}{g}\phi_t^{(1)}\frac{\partial}{\partial z}\left(\phi_{tt}^{(2)}+g\phi_z^{(2)}\right)+\frac{2}{g}\phi_t^{(1)}\frac{\partial}{\partial z}\left(\nabla\phi^{(1)}\cdot\nabla\phi_t^{(1)}\right)\\&-\frac{1}{g}\left(\frac{1}{g}\phi_t^{(1)}\phi_{tz}^{(1)}-\frac{1}{2}\nabla\phi^{(1)}\cdot\nabla\phi^{(1)}\right)\frac{\partial}{\partial z}\left(\phi_{tt}^{(1)}+g\phi_z^{(1)}\right)\\&-\frac{1}{2g^2}\left(\phi_t^{(1)}\right)^2\frac{\partial^2}{\partial z^2}\left(\phi_{tt}^{(1)}+g\phi_z^{(1)}\right).\end{aligned} \tag{7}$$

Eq. (5) holds if the terms multiplied by ε^i vanish for each $i=1,2,\ldots$ As a result of this and defining $F^{(1)}:=0$, the equations for the computation of the first three velocity potentials $\phi^{(i)}$, $i=1,2,3$, can be derived to be

$$\phi_{xx}^{(i)}+\phi_{yy}^{(i)}+\phi_{zz}^{(i)}=0,\qquad \text{for}\quad -h\le z\le 0, \tag{8a}$$

$$\phi_z^{(i)}=0,\qquad \text{for}\quad z=-h, \tag{8b}$$

$$\nabla\phi^{(i)}\cdot\mathbf{n}=\mathbf{u}^{(i)}\cdot\mathbf{n},\qquad \text{for}\quad (x,y,z)\in S_{\mathrm{B}0}, \tag{8c}$$

$$\phi_{tt}^{(i)}+g\phi_z^{(i)}=F^{(i)},\qquad \text{for}\quad z=0. \tag{8d}$$

Note that the BC (8c) is not formulated at the actual wetted surface of the body S_B, but at $S_{\mathrm{B}0}$. Here, $S_{\mathrm{B}0}$ denotes all points at the surface of the body S_B, which are located below the still water level. The reason to use $S_{\mathrm{B}0}$ in the BC (8c) is that the velocity potentials $\phi_\mathrm{B}^{(i)}$ are only calculated below the rest position of the sea surface, i. e. for $z\le 0$.

Equation (8d) has been stated several times in the literature, see e.g. (Eatock Taylor and Hung, 1987; Malenica and Molin, 1995; Rahman et al., 1999). An advantage of using the BC (8d) instead of the BC (3) is that the BC (8d) is linear with respect to the corresponding highest-order velocity potential. Moreover, the lower-order velocity potentials are independent of the higher-order ones, which allows an computation of the velocity potentials $\phi^{(i)}$, $i=1,2,3$, in increasing order.

Having computed the velocity potentials $\phi^{(i)}$, the corresponding sea surface displacements $\eta^{(i)}$ from Eq. (4b) can be computed using the formulas given in Appendix A.

2.3. Computation of the body disturbance and the FSI

In general, the dynamics of the incoming water waves are disturbed by the presence and motion of the floating body. To compute this disturbance, the total velocity potential ϕ is divided into two parts. The first part is the velocity potential ϕ_0 of the incoming water waves, which are not disturbed by the presence of the body. The second part is the velocity potential ϕ_B corresponding to the body disturbance, taking into account diffraction and radiation effect of the body, see e.g. (Bai and Teng, 2013). Both velocity potentials, ϕ_0 and ϕ_B, are expanded according to the Stokes expansion procedure given in Eq. (4), i.e.

$$\phi=\phi_0+\phi_\mathrm{B}=\varepsilon(\phi_0^{(1)}+\phi_\mathrm{B}^{(1)})+\varepsilon^2(\phi_0^{(2)}+\phi_\mathrm{B}^{(2)})+\varepsilon^3(\phi_0^{(3)}+\phi_\mathrm{B}^{(3)})+O(\varepsilon^4). \tag{9}$$

Note that the velocity potential ϕ_B disappears in the absence of a body, which results in $\phi=\phi_0$. This means that the velocity potentials $\phi_0^{(i)}$ have to satisfy the Eqs. (8a), (8b), and (8d). Some analytical solutions for $\phi_0^{(1)}$ and $\phi_0^{(2)}$ are presented in Section 2.4.

If the incident velocity potentials $\phi_0^{(i)}$ are known, the corresponding equations for the velocity potentials $\phi_\mathrm{B}^{(i)}$ can be formulated by substituting $\phi^{(i)}=\phi_0^{(i)}+\phi_\mathrm{B}^{(i)}$ into Eq. (8). In Fig. 1, the resulting nonlinear scheme for the computation of the total velocity potential $\phi=\phi_0+\phi_\mathrm{B}$ is summarized. All corresponding equations for the calculation of the first three components of the velocity potentials ϕ, ϕ_0, and ϕ_B are also presented there.

When computing $\phi_\mathrm{B}^{(i)}$, it has to be noted that a radiation condition must be formulated that determines the behavior of $\phi_\mathrm{B}^{(i)}$ far away from the floating body. However, in this work, the velocity potentials $\phi_\mathrm{B}^{(i)}$ are computed numerically using the scheme sketched in Section 5. Instead of considering radiation conditions, suitable absorbing BCs at the end of the spatial domain are formulated here, see Section 5.2.

After computing the total velocity potential ϕ, the hydrodynamic pressure $p=p(\phi)$ acting on the wetted surface of the mechanical structure can be computed using Bernoulli's formula. Afterward, the hydrodynamic loads acting on the mechanical structure and the dynamics of

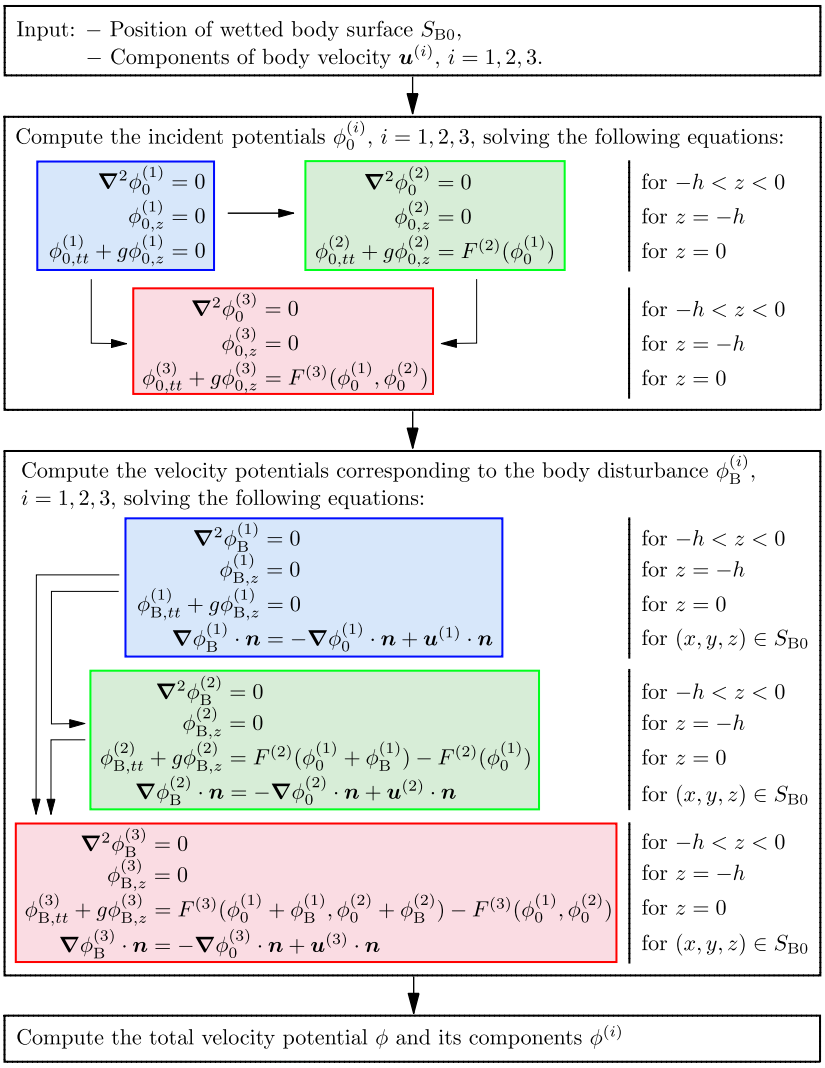

Fig. 1. Schematic representation of the method for calculating the total velocity potential ϕ, which is disturbed by the presence and motion of a mechanical structure, and its components $\phi^{(1)}$, $\phi^{(2)}$, and $\phi^{(3)}$.

the mechanical structure can be determined. In this way, the FSI between a mechanical structure and water waves prescribed by the incident velocity potentials $\phi_0^{(1)}$, $\phi_0^{(2)}$, and $\phi_0^{(3)}$ can be calculated.

2.4. Analytical solutions for higher-order Stokes waves

The incident velocity potentials $\phi_0^{(1)}$, $\phi_0^{(2)}$, and $\phi_0^{(3)}$ can be computed by solving the equations summarized in Fig. 1. In general, this can be done numerically. However, for the case of regular and random waves, analytical solutions for $\phi_0^{(1)}$ and $\phi_0^{(2)}$ are known. These solutions are introduced in this section for a later comparison with the NLS, which will be introduced in Section 3. Based on the Stokes perturbation expansion from Eq. (4), the incoming water waves considered in this section are called Stokes waves.

For incoming regular waves, the first-order component of the sea surface displacement η is given by $\varepsilon\eta^{(1)}(x, y, t) = A\cos(\theta)$ and the corresponding velocity potentials $\phi_0^{(1)}$ and $\phi_0^{(2)}$ are given by

$$\begin{aligned}\varepsilon\phi_0^{(1)}(x, y, z, t) &= \frac{gA}{\omega}\frac{\cosh(k(z+h))}{\cosh(kh)}\sin(\theta),\\ \varepsilon^2\phi_0^{(2)} &= \frac{3\omega A^2}{8}\frac{\cosh(2k(z+h))}{\sinh^4(kh)}\sin(2\theta),\end{aligned} \tag{10}$$

whereby $\theta = k(\cos(\chi)x + \sin(\chi)y) - \omega t + \beta$. Here, A is the wave amplitude, ω is the wave frequency, k is the wave number, χ is the angle between the wave direction and the x-axis, and β is a phase shift. Furthermore, k and ω are related by the dispersion relation $\omega^2 = kg\tanh(kh)$.

Next, random waves are considered. The first-order sea surface displacement $\varepsilon\eta^{(1)}$ of an irregular short-crested sea can be written in the absence of any structure as the sum of many regular water waves and is given by

$$\begin{aligned}\varepsilon\eta^{(1)}(x, y, t) &= \sum_{m=1}^{M} a_m\cos(\theta_m), \quad \text{with}\\ \theta_m &= k_m(\cos(\chi_m)x + \sin(\chi_m)y) - \omega_m t + \beta(\omega_m, \chi_m).\end{aligned} \tag{11}$$

Here, β is a random phase shift, which is uniformly distributed in $[0, 2\pi)$. Furthermore, the amplitudes a_m depend on the underlying sea state given by the corresponding one-sided spectral density $S(\omega)$ and the spread function $D(\chi)$, see e.g. (Mitsuyasu et al., 1975; Clauss et al., 1988). The incident velocity potentials $\varepsilon\phi_0^{(1)}$ and $\varepsilon^2\phi_0^{(2)}$ corresponding to the sea surface displacement from Eq. (11) can be found, for example, in (Sharma and Dean, 1979)

When computing the corresponding second-order sea surface displacement $\eta^{(2)}$ and velocity potential $\phi^{(2)}$, interactions between the M components of the first-order sea surface displacement $\eta^{(1)}$ have to be

considered. The number of interactions is given by M^2. Therefore, calculating all nonlinear interactions becomes increasingly inefficient when the number of regular components M in the first-order irregular sea state grows. As a result, a Stokes theory of higher order needs much computation time in the presence of random waves (Slunyaev et al., 2014). In the following sections, it is investigated how the FSI with nonlinear water waves can be computed more efficiently using the nonlinear Schrödinger equation.

3. Nonlinear Schrödinger equation

The nonlinear Schrödinger equation (NLS) is a partial differential equation (PDE) that can be used to describe weakly nonlinear deep water waves with a narrow spectral bandwidth and a moderate wave steepness (Dysthe, 1979; Osborne, 2010; Witt, 2019). Since solutions of the NLS can be computed very efficiently, the NLS is used firstly in this work to calculate the nonlinear FSI.

First, the most important equations regarding the NLS are introduced in Section 3.1. Afterward, the derivation of the NLS is briefly outlined in Section 3.2 to understand how the NLS is related to the wave theory presented in Section 2.2. Finally, different solutions of the NLS are presented in Section 3.3 and 3.4.

3.1. General overview about equations

All formulas presented here result from the derivations given in Section 3.2. In terms of the coordinates $X := \varepsilon x$ and $T := \varepsilon t$, the NLS is given by

$$\mathrm{i}(\psi_T + c_{\mathrm{gr}}\psi_X) = \nu\psi_{XX} + \delta|\psi|^2\psi, \tag{12}$$

whereby $\nu = \varepsilon\frac{\omega_0}{8k_0^2}$, $\delta = \varepsilon\frac{1}{2}\omega_0 k_0^2$, and $c_{\mathrm{gr}} = \frac{\omega_0}{2k_0}$. In addition, $\psi = \psi(X,T) \in \mathbb{C}$ describes the wave envelope of the oscillations of a carrier wave with wave frequency ω_0, wave number k_0, and group velocity c_{gr}. Here, ω_0 and k_0 are linked by the linear dispersion relation in deep water, i. e. $\omega_0^2 = gk_0$.

The NLS yields the complex wave envelope ψ, from which the sea surface displacement $\eta(x,t)$ of the corresponding water waves can be computed by, see Section 3.2,

$$\eta(x,t) = \mathrm{Re}\Bigg\{\varepsilon\psi E + \frac{1}{2}\varepsilon^2 k_0\psi^2E^2 + \varepsilon^3\left[\frac{3}{8}k_0^2\psi^3E^3 - \frac{1}{2}\mathrm{i}\psi\psi_X E^2 + \frac{\omega_0}{2g}\frac{\partial}{\partial T}\left(\mathcal{H}\left(|\psi|^2\right)\right)\right]\Bigg\} + O(\varepsilon^4). \tag{13}$$

Here, it is $E = \mathrm{e}^{\mathrm{i}(k_0x-\omega_0t)}$ and $\mathcal{H}$ denotes the Hilbert transform, which is applied with respect to the coordinate X.

Having computed the wave envelope ψ solving the NLS (12), the velocity potential ϕ of the corresponding water waves follows as, see Section 3.2,

$$\phi(x,z,t) = \mathrm{Re}\Bigg\{\left[-\frac{\mathrm{i}\varepsilon\omega_0}{k_0}\widetilde{\psi} + \frac{\varepsilon^2\omega_0}{2k_0^2}\widetilde{\psi}_X + \varepsilon^3\left(\frac{\mathrm{i}k_0\omega_0}{8}\widetilde{C} + \frac{3\mathrm{i}\omega_0}{8k_0^3}\widetilde{\psi}_{XX}\right)\right]E\mathrm{e}^{k_0z} + 2\varepsilon^2\bar{\phi}_0 + 2\varepsilon^3\bar{\phi}_1\Bigg\} + O(\varepsilon^4). \tag{14}$$

Eq. (14) is the corrected version of the formula from Carter et al. (2020), whereby $\widetilde{\psi}(X,Z,T) := \psi(X - \mathrm{i}Z, T)$, $C := |\psi|^2\psi$, $\widetilde{C}(X,Z,T) := C(X - \mathrm{i}Z,T)$, and $Z := \varepsilon z$, see (Hollm et al., 2024). Furthermore, $\bar{\phi}_0 = \bar{\phi}_0(X,Z,T)$ and $\bar{\phi}_1 = \bar{\phi}_1(X,Z,T)$ are velocity potentials representing a mean flow of the water waves. Using the Fourier transform $\mathcal{F}$ and its inverse $\mathcal{F}^{-1}$, which are applied with respect to the coordinate X, the velocity potential $\bar{\phi}_0$ is given by

$$\mathrm{Re}\left\{2\bar{\phi}_0\right\} = \bar{\phi}_0 + \bar{\phi}_0^* = \mathcal{F}^{-1}\left(\frac{1}{2}\mathrm{i}\omega_0\,\mathrm{sgn}(k)\mathcal{F}\left(|\psi|^2\right)\mathrm{e}^{|k|Z}\right), \tag{15}$$

whereby $\bar{\phi}_0^*$ denotes the complex conjugate of $\bar{\phi}_0$. As is shown in Section 4, the velocity potential $\bar{\phi}_1$ is not needed for the computational method formulated in this work to calculate the FSI. Therefore, $\bar{\phi}_1$ is not further specified here.

3.2. Derivation of the NLS

To understand how the theory of the NLS is related to the wave theory presented in Section 2.2, the derivation of the NLS is shortly outlined. The derivation is based on (Dysthe, 1979; Mei, 1983; Carter et al., 2020). Only deep water waves are considered in the following, which propagate in the x-direction.

The nonlinear governing equations of fluid motion are given by Eq. (1). When approximating Eq. (1) in Section 2.2, it has been first used that the two BCs (1b) and (1c) at the free sea surface at $z = \eta$ can be combined to one single BC at $z = \eta$. Considering deep water waves and using the combined BC at $z = \eta$ together with the Eqs. (1a), (1c), and (1d), the governing equations of fluid motion from Eq. (1) result in

$$\boldsymbol{\nabla}^2\phi = \phi_{xx} + \phi_{zz} = 0, \text{ for } z \le \eta(x,t), \tag{16a}$$

$$\phi_{tt} + g\phi_z + 2\boldsymbol{\nabla}\phi\cdot\boldsymbol{\nabla}\phi_t + \frac{1}{2}\boldsymbol{\nabla}\phi\cdot\boldsymbol{\nabla}(\boldsymbol{\nabla}\phi\cdot\boldsymbol{\nabla}\phi) = 0, \text{ for } z = \eta(x,t), \tag{16b}$$

$$\phi_t + \frac{1}{2}\boldsymbol{\nabla}\phi\cdot\boldsymbol{\nabla}\phi + g\eta = 0, \text{ for } z = \eta(x,t), \tag{16c}$$

$$\phi_z \to 0, \text{ for } z \to -\infty. \tag{16d}$$

In the next step, Taylor series expansions are used to expand the BCs (16b) and (16c) from $z = \eta(x,t)$ to $z = 0$. Looking only at the terms up to third order in the product of ϕ, η, and their derivatives, the expanded equations at $z = 0$ become

$$\phi_{tt} + g\phi_z + \eta\frac{\partial}{\partial z}\left[\phi_{tt} + g\phi_z\right] + 2\boldsymbol{\nabla}\phi\cdot\boldsymbol{\nabla}\phi_t + \frac{1}{2}\eta^2\frac{\partial^2}{\partial z^2}\left[\phi_{tt} + g\phi_z\right] + \eta\frac{\partial}{\partial z}\left[2\boldsymbol{\nabla}\phi\cdot\boldsymbol{\nabla}\phi_t\right] + \frac{1}{2}\boldsymbol{\nabla}\phi\cdot\boldsymbol{\nabla}(\boldsymbol{\nabla}\phi\cdot\boldsymbol{\nabla}\phi) = 0, \tag{17a}$$

$$-g\eta = \phi_t + \eta\phi_{tz} + \frac{1}{2}\boldsymbol{\nabla}\phi\cdot\boldsymbol{\nabla}\phi + \frac{1}{2}\eta^2\phi_{tzz} + \eta\frac{\partial}{\partial z}\left[\frac{1}{2}\boldsymbol{\nabla}\phi\cdot\boldsymbol{\nabla}\phi\right]. \tag{17b}$$

These equations have also been presented, for example, in (Mei, 1983). Following (Dysthe, 1979; Carter et al., 2020), generalized Stokes perturbation expansions of the form

$$\phi(x,z,t) = \varepsilon^2\bar{\phi} + \varepsilon A_1\mathrm{e}^{k_0z+\mathrm{i}\vartheta} + \varepsilon^2A_2\mathrm{e}^{2(k_0z+\mathrm{i}\vartheta)} + \cdots + \text{c.c.}, \tag{18a}$$

$$\eta(x,t) = \varepsilon^3\bar{\eta} + \varepsilon B\mathrm{e}^{\mathrm{i}\vartheta} + \varepsilon^2B_2\mathrm{e}^{2\mathrm{i}\vartheta} + \varepsilon^3B_3\mathrm{e}^{3\mathrm{i}\vartheta} + \cdots + \text{c.c.} \tag{18b}$$

are used. Here, it is $\vartheta = k_0x - \omega_0t$, $\varepsilon = k_0A_0$ represents the steepness of the carrier wave with wave number k_0 and a typical wave amplitude A_0, and c.c. represents the complex conjugate. Finally, as it is described by Carter et al. (2020), it is assumed

$$\bar{\phi} = \bar{\phi}(X,Z,T) = \bar{\phi}_0(X,Z,T) + \varepsilon\bar{\phi}_1(X,Z,T) + \varepsilon^2\bar{\phi}_2(X,Z,T) + \dots, \tag{19a}$$

$$A_j = A_j(X,Z,T) = A_{j0}(X,Z,T) + \varepsilon A_{j1}(X,Z,T) + \varepsilon^2A_{j2}(X,Z,T) + \dots, \text{ for } j = 1,2,3,\dots, \tag{19b}$$

$$\bar{\eta} = \bar{\eta}(X,T) = \bar{\eta}_0(X,T) + \varepsilon\bar{\eta}_1(X,T) + \varepsilon^2\bar{\eta}_2(X,T) + \dots, \tag{19c}$$

$$B = B(X,T), \tag{19d}$$

$$B_j = B_j(X,Z,T) = B_{j0}(X,Z,T) + \varepsilon B_{j1}(X,Z,T) + \varepsilon^2B_{j2}(X,Z,T) + \dots, \quad \text{for } j = 2,3,4,\dots \tag{19e}$$

The expressions from Eqs. (18) and (19) are substituted into the Laplace Eq. (16a) and the BCs (17a) and (17b) at $z = 0$. This yields terms of various orders in ε and $\mathrm{e}^{k_0z\pm\mathrm{i}\vartheta}$, which are analyzed separately. The resulting PDEs and BCs at $z = 0$ for the unknowns A_{ij} and $\bar{\phi}_i$, which appear in Eq. (19) up to the order $O(\varepsilon^3)$, are formulated in Appendix B. Also, the corresponding solutions for all A_{jk}, B_{jk}, $\bar{\phi}_j$, and $\bar{\eta}_j$, which appear in Eq. (19) up to the order $O(\varepsilon^3)$, are given in Appendix B in terms of B.

It remains to calculate the function B. For this, the solutions for A_{ij} and $\bar{\phi}_0$ given in Appendix B are substituted into Eq. (18a). Substituting the resulting expression for the velocity potential ϕ into BC (3) and then considering only the terms up to order $O(\varepsilon^3)$, it is found that B has to satisfy

$$\mathrm{i}\varepsilon^2\left(B_T + \frac{\omega_0}{2k_0}B_X\right) = \varepsilon^3\left(\frac{\omega_0}{8k_0^2}B_{XX} + 2\omega_0 k_0^2 B|B|^2\right). \tag{20}$$

After solving Eq. (20), the corresponding velocity potential ϕ and sea surface displacement η can be calculated by substituting the Eqs. (B.2)-(B.5) into Eq. (18).

The resulting expressions for η and ϕ can sightly be simplified by substituting $\psi(X,T) = 2B(X,T)$. In this way, the NLS (12) is obtained by substituting $\psi(X,T) = 2B(X,T)$ into Eq. (20). The resulting formulas for the sea surface displacement η and velocity potential ϕ are given by Eq. (13) and Eq. (14), respectively.

It has to be noted that only the terms from Eq. (18) up to the order $O(\varepsilon^3)$ have been considered and calculated in this section. Also the nonlinear BC (3) at $z = 0$ has been approximated accurately up to the order $O(\varepsilon^3)$. Terms of order $O(\varepsilon^4)$ and higher have been neglected in this section. Therefore, the NLS is accurate to the third order in the wave steepness ε. This has also been stated, for example, in (Shemer and Dorfman, 2008).

3.3. Analytical solutions of the NLS

In contrast to the nonlinear governing equations of fluid motion from Eq. (1), several analytical solutions of the NLS (12) are well-known and closed-form expressions are available, see e.g. (Peregrine, 1983; Osborne, 2010; Slunyaev et al., 2013; Carter et al., 2020) and the references therein. In the following, two of these solutions are presented and discussed. In later sections, these solutions are used to compute the FSI between nonlinear water waves and mechanical structures.

3.3.1. Plane-wave solution

The plane-wave solution of the NLS with constant amplitude $\psi_0 \in \mathbb{R}$ is given by

$$\psi(X,T) = \psi_0 \mathrm{e}^{-\mathrm{i}\delta\psi_0^2 T}, \tag{21}$$

see e.g. (Carter et al., 2020). This solution of the NLS can be used present regular water waves. Substituting ψ from Eq. (21) into Eqs. (13) and (14), it is found that the corresponding sea surface displacement η and velocity potential ϕ oscillate in time with the wave frequency ω_{NLS}, which is given by

$$\omega_{\mathrm{NLS}}^2 = \left(\omega_0(1 + \frac{1}{2}\varepsilon^2 k_0^2\psi_0^2)\right)^2 = k_0 g(1 + \varepsilon^2 k_0^2\psi_0^2) + \mathcal{O}(\varepsilon^4) \tag{22}$$

with $\omega_0^2 = k_0 g$. This shows that the NLS recovers the nonlinear dispersion relation, in which the wave frequency depends on the amplitude $A = \varepsilon\psi_0$ of the corresponding water waves.

3.3.2. Peregrine breather solution

One important analytical solution of the NLS (12) has been found by Peregrine (1983) and is known as the Peregrine breather solution. It is given by

$$\psi(X,T) = \psi_0\left(\frac{4\nu\left(1 - 2\mathrm{i}\delta\psi_0^2 T\right)}{\nu\left[1 + \left(2\delta\psi_0^2 T\right)^2\right] + 2\delta\psi_0^2\left(X - c_{\mathrm{gr}}T - X_{\mathrm{s}}\right)^2} - 1\right)\mathrm{e}^{-\mathrm{i}\delta\psi_0^2 T}. \tag{23}$$

Fig. 2a shows the amplitude $|\psi|$ of the Peregrine breather solution for $\psi_0 = 1.5\,\mathrm{m}$ $k_0 = 0.5\,\mathrm{m}^{-1}$, $\varepsilon = 0.1$, and $X_{\mathrm{s}} = c_{\mathrm{gr}}\varepsilon \cdot 200\,\mathrm{s} = 44.29\,\mathrm{m}$. The spatial shift X_{s} is chosen so that the Peregrine breather solution reaches its peak value for $t = -200\,\mathrm{s}$ at $x = 0\,\mathrm{m}$, see Fig. 2a. Fig. 2b shows the corresponding sea surface displacement $\eta = \mathrm{Re}\{\varepsilon\psi E\}$ at $x = X_{\mathrm{s}}/\varepsilon = 442.9\,\mathrm{m}$, where the Peregrine breather solution reaches its maximum peak amplitude over time. For better illustration, the position $x = 442.9\,\mathrm{m}$ is marked in Fig. 2a.

In Figs. 2a and 2b, it is shown that the Peregrine breather solution is localized both in time and space. Being doubly localized, the Peregrine breather solution describes a unique wave event in which large amplitude waves seem to come out of nowhere and disappear without a trace (Chabchoub et al., 2012). In different studies, it has been conjectured that the Peregrine is a prototype of rogue waves in the ocean, see e.g. (Dysthe and Trulsen, 1999; Shrira and Geogjaev, 2010; Dostal et al., 2020).

3.4. Perturbation of solutions of the NLS

In contrast to the water waves that correspond to the presented analytical solutions of the NLS, real water waves are irregular. In this section, an approach is presented that enables the computation of irregular sea states using the NLS by perturbing analytical solutions of the NLS. This makes it possible to describe a method in the next section that employs the NLS to compute the FSI between a structure and random nonlinear water waves.

The idea of the approach presented in this section is to consider the wave envelope ψ of an analytical solution of the NLS (12) at some time-point T_0 and to perturb the value of $\psi(X,T_0)$ using an irregular sea surface. Using this perturbed value of $\psi(X,T_0)$ as initial condition, the corresponding temporal behavior of the perturbed wave envelope can be computed by solving the NLS (12) numerically over time. Note that solutions ψ of the NLS (12) can be computed numerically very efficiently employing, for example, the relaxation pseudo-spectral (ReSP) scheme used in (Antoine and Duboscq, 2015; Hollm et al., 2024).

Let $\eta_{\mathrm{LC}}(x,t)$ be the sea surface displacement of a long-crested random water wave, which can be computed using Eq. (11) with $\theta_m = 0$ for $m = 1,\dots,M$. With that, a perturbed initial condition, which is based on some analytical solution ψ of the NLS (12), is given by

$$\psi_{0,\mathrm{perturb}}(X) = \left(1 + \frac{\eta_{\mathrm{LC}}(x(X),0)}{|\psi_0(X)|}\right)\psi_0(X), \quad \text{with } x(X) = X/\varepsilon, \tag{24}$$

whereby $\psi_0(X) = \psi(X,T_0)$. This approach for computing an perturbed initial condition $\psi_{0,\mathrm{perturb}}$ has originally been presented in (Hollm et al., 2021, 2022a). Using the approach from Eq. (24), the amplitude of $\psi_0(X)$ is perturbed by $\eta_{\mathrm{LC}}(x(X),0)$.

Fig. 3 illustrates the effect of an irregular perturbation on a Peregrine breather solution using Eq. (24). It can be seen that the used sea surface displacement η_{LC} can be found directly in the amplitude of the perturbed initial condition $\psi_{0,\mathrm{perturb}}$.

4. Computation of the FSI using the NLS

In this section, it is developed how the NLS can be used to compute the FSI between a structure and nonlinear water waves. Furthermore, the corresponding order of accuracy of the proposed computational method to calculate the FSI is analyzed.

In Section 2.3, it is shown that the computation of the nonlinear FSI includes the computation of the incident velocity potential ϕ_0 and the velocity potential corresponding to the body disturbance ϕ_{B}. Having the solution ψ of the NLS (12), the corresponding incident velocity potential ϕ_0 can be computed using Eq. (14). Comparing the Stokes' expansion from Eq. (4a) with the velocity potential from Eq. (14), it can be seen that the first three incident velocity potentials $\phi_0^{(i)}$, $i = 1,2,3$, corresponding to the NLS are given by

$$\phi_0^{(1)}(x,z,t) = \mathrm{Re}\left\{-\frac{\mathrm{i}\omega_0}{k_0}\widetilde{\psi}E\mathrm{e}^{k_0 z}\right\}, \tag{25a}$$

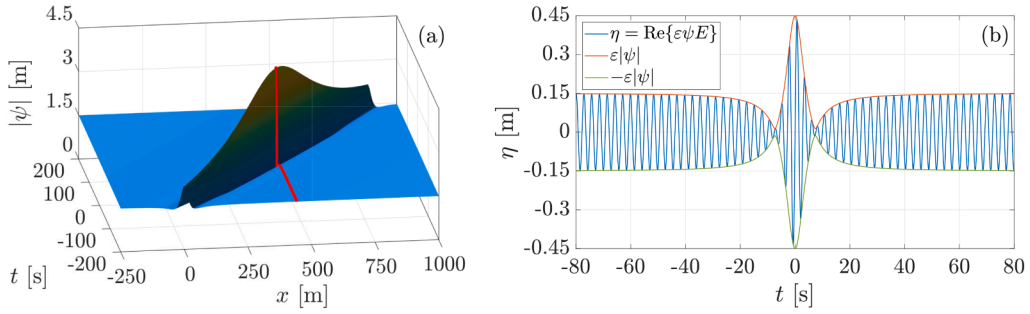

Fig. 2. (a): Amplitude of wave envelope ψ of the Peregrine breather solution. (b): Corresponding sea surface displacement $\eta = \mathrm{Re}\{\varepsilon\psi E\}$.

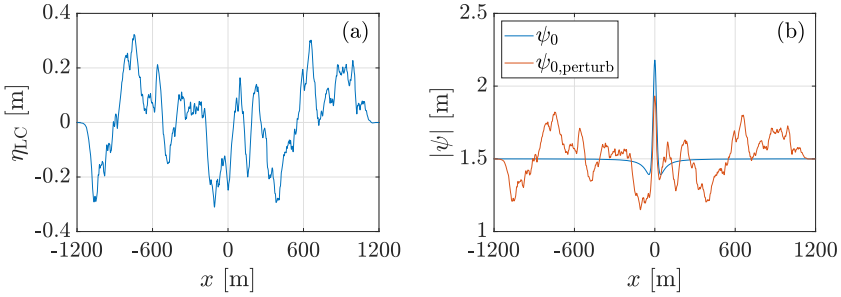

Fig. 3. (a): Example of a random water wave generated using a Pierson-Moskowitz spectrum with peak frequency $\omega_p = 0.25\,\mathrm{rad/s}$ and significant wave height $H_s = 1\,\mathrm{m}$. (b): Peregrine breather solution with parameters $k_0 = 0.5\,\mathrm{m}^{-1}$, $\psi_0 = 1.5\,\mathrm{m}$, $\varepsilon = 0.1$ at time $T_0 = -20\,\mathrm{s}$ with and without the irregular perturbation illustrated in (a).

$$\phi_0^{(2)}(x,z,t) = \mathrm{Re}\left\{\frac{\omega_0}{2k_0^2}\widetilde{\psi}_X E\mathrm{e}^{k_0 z} + 2\bar{\phi}_0\right\}, \tag{25b}$$

$$\phi_0^{(3)}(x,z,t) = \mathrm{Re}\left\{\left(\frac{\mathrm{i}k_0\omega_0}{8}\widetilde{C} + \frac{3\mathrm{i}\omega_0}{8k_0^3}\widetilde{\psi}_{XX}\right)E\mathrm{e}^{k_0 z} + 2\bar{\phi}_1\right\}. \tag{25c}$$

For the computation of $\widetilde{\psi}(X,Z,T) = \psi(X - \mathrm{i}Z, T)$ and $\widetilde{C}(X,Z,T) = C(X - \mathrm{i}Z, T)$, it has to be noted that ψ and C are unknown at the location $X - \mathrm{i}Z$ if no analytical expression for ψ is given. This is the general case, for example, when the perturbation approach presented in Section 3.4 is used to calculate irregular sea states. However, $\widetilde{\psi}$ can be determined by solving the complex transport equation

$$\widetilde{\psi}_Z = -\mathrm{i}\widetilde{\psi}_X, \quad \text{for } Z < 0, \tag{26a}$$

$$\widetilde{\psi} = \psi, \quad \text{for } Z = 0. \tag{26b}$$

An analog complex transport equation can be solved to compute $\widetilde{C}$.

In summary, after solving the NLS (12) for the wave envelope ψ, the first three incident velocity potentials $\phi_0^{(i)}$ can be computed using Eq. (25). Afterward, the body disturbance velocity potentials $\phi_B^{(i)}$ can be calculated numerically solving the PDEs and BCs summarized in Fig. 1. Compared to the Stokes waves introduced in Section 2.4, the NLS-based method for the computation of the velocity potentials $\phi_0^{(i)}$ avoids the explicit computation of nonlinear wave-wave interactions, as nonlinear wave effects are considered directly when solving the NLS. This significantly reduces the computational effort. Thus, the NLS approach provides a more efficient framework for calculating the nonlinear velocity potentials $\phi_0^{(i)}$ relevant to the FSI analysis than the approach presented in Section 2.4.

In the following, several remarks are made about the incident velocity potentials $\phi_0^{(i)}$ from Eq. (25) and the computation of the corresponding FSI.

4.1. Mean velocity potential $\bar{\phi}_1$

In this section, it is explained why the mean velocity potential $\bar{\phi}_1$ from Eq. (14) is not needed in the formulation of the FSI considered in this work. The nonlinear FSI is computed using the method presented in Section 2.3 and Fig. 1. Going through the equations summarized in Fig. 1, it can be observed that the incident velocity potentials $\phi_0^{(i)}$ appear in these equations only in combination with derivatives with respect to x, z, and t. However, the mean potential $\bar{\phi}_1$ depends only on $T = \varepsilon t$, $X = \varepsilon x$, and $Z = \varepsilon z$. At this point, it holds

$$\bar{\phi}_{1,t} = \varepsilon\bar{\phi}_{1,T}, \quad \bar{\phi}_{1,x} = \varepsilon\bar{\phi}_{1,X}, \quad \bar{\phi}_{1,z} = \varepsilon\bar{\phi}_{1,Z}. \tag{27}$$

Since $\bar{\phi}_1$ is of order $O(\varepsilon^3)$, the derivatives $\bar{\phi}_{1,t}$, $\bar{\phi}_{1,x}$, and $\bar{\phi}_{1,z}$ are of order $O(\varepsilon^4)$. Therefore, considering $\bar{\phi}_1$ only affects the nonlinear FSI of order $O(\varepsilon^4)$. However, as has been shown in Section 3.2, the NLS models water waves accurately up to the order $O(\varepsilon^3)$. Thus, the maximal achievable order of accuracy in the computation of the FSI with nonlinear water waves using the NLS is $O(\varepsilon^3)$. As $\bar{\phi}_1$ only affects the nonlinear FSI of order $O(\varepsilon^4)$, $\bar{\phi}_1$ is not specified here and will not be considered in the further course of this work.

4.2. Boundary condition at $z = -h$

In the formulation of the NLS, only deep water waves are considered. Consequently, the value of $\phi_{0,z}$ vanishes only for $z \to -\infty$, see Eq. (16d). In contrast, in the fundamental equations for the computation of the FSI presented in Fig. 1, it is assumed that the value of $\phi_{0,z}^{(i)}$ vanishes at $z = -h$. Since the incident velocity potentials $\phi_0^{(i)}$ corresponding to the NLS do not satisfy this BC for any $h < \infty$, their use introduces errors in the computation of the FSI. However, due to the exponential dependence of the incident velocity potentials $\phi_0^{(i)}$ in z, see Eq. (25), this error becomes small for a large water depth h. Therefore, when computing the FSI using the NLS, the water depth h is always chosen to satisfy the deep water condition, i. e. $h > \frac{1}{2}\lambda = \frac{\pi}{k_0}$, where λ is the wave length of the incoming water waves.

4.3. Boundary condition at $z = 0$

The next remark refers to the BC at the still water surface, which is located at $z = 0$. The corresponding BC is given in Eq. (8d) and has to

be satisfied by $\phi_0^{(i)}$, $i = 1, 2, 3$. Substituting the velocity potentials $\phi_0^{(1)}$, $\phi_0^{(2)}$, and $\phi_0^{(3)}$ from Eq. (25) into the BC (8d) at $z = 0$ yields

$$\varepsilon\left(\phi_{0,tt}^{(1)} + g\phi_{0,z}^{(1)}\right) = O(\varepsilon^3), \tag{28a}$$

$$\varepsilon^2\left(\phi_{0,tt}^{(2)} + g\phi_{0,z}^{(2)} - F^{(2)}(\phi_0^{(1)})\right) = O(\varepsilon^4), \tag{28b}$$

$$\varepsilon^3\left(\phi_{0,tt}^{(3)} + g\phi_{0,z}^{(3)} - F^{(3)}(\phi_0^{(1)}, \phi_0^{(2)})\right) = O(\varepsilon^3). \tag{28c}$$

Therefore the incident velocity potentials $\phi_0^{(1)}$, $\phi_0^{(2)}$, and $\phi_0^{(3)}$ from Eq. (25) do not exactly satisfy the BC (8d). This is the result of a simplification that has been used in the derivation of BC (8d). The BC (8d) has been derived by substituting the velocity potential $\phi = \varepsilon\phi^{(1)} + \varepsilon^2\phi^{(2)} + \varepsilon^3\phi^{(3)} + O(\varepsilon^4)$ into the nonlinear BC (3) at $z = 0$. Then it has been used that the resulting Eq. (5) holds if each term multiplied by ε^i, $i = 1, 2, 3, \ldots$, vanishes by itself. In contrast, however, the NLS has been derived by substituting the generalized Stokes perturbation expansion of ϕ from Eq. (18a) into the BC (3). Therefore, the incident velocity potential $\phi_0 = \varepsilon\phi_0^{(1)} + \varepsilon^2\phi_0^{(2)} + \varepsilon^3\phi_0^{(3)}$ satisfies the BC (3) up to an error of order $O(\varepsilon^4)$. In other words, the incident velocity potentials of the NLS do not fulfill all terms multiplied by ε^i separately, but the sum of all terms multiplied by the different exponents ε^i, yielding

$$\begin{aligned}\varepsilon\left(\phi_{0,tt}^{(1)} + g\phi_{0,z}^{(1)}\right) + \varepsilon^2\left(\phi_{0,tt}^{(2)} + g\phi_{0,z}^{(2)} - F^{(2)}(\phi_0^{(1)})\right) \\ + \varepsilon^3\left(\phi_{0,tt}^{(3)} + g\phi_{0,z}^{(3)} - F^{(3)}(\phi_0^{(1)}, \phi_0^{(2)})\right) = O(\varepsilon^4).\end{aligned} \tag{29}$$

In summary, the velocity potential $\phi_0 = \varepsilon\phi_0^{(1)} + \varepsilon^2\phi_0^{(2)} + \varepsilon^3\phi_0^{(3)}$ satisfies the BC (3) up to an error of order $O(\varepsilon^4)$ and thus up to an accuracy of order $O(\varepsilon^3)$. On the other side, the individual incident velocity potentials $\phi_0^{(i)}$ from Eq. (25) do not satisfy the BC (8d) up to an error of order $O(\varepsilon^4)$, see Eq. (28). However, using the method presented in Section 2.3 and Fig. 1 to compute the FSI, a corresponding accuracy of order $O(\varepsilon^3)$ can only be obtained if the incident velocity potentials $\phi_0^{(i)}$ satisfy the BC (8d). Therefore, if the nonlinear FSI is computed for waves corresponding to the NLS, an accuracy of order $O(\varepsilon^3)$ cannot be obtained using the method presented in Section 2.3 and Fig. 1.

However, considering Eq. (28), it can be seen that all incident velocity potentials $\phi_0^{(i)}$ from Eq. (25) satisfy the BC (8d) up to an error of order $O(\varepsilon^3)$ and thus up to an accuracy of order $O(\varepsilon^2)$. Using the method presented in Section 2.3 and Fig. 1, this shows that it is possible to compute the nonlinear FSI between nonlinear water waves corresponding to the NLS and a mechanical structure if a modeling error of order $O(\varepsilon^3)$ is accepted.

It has to be noted that the incident velocity potential $\phi_0^{(1)}$ satisfies the first-order BC (28a) only up to an error of order $O(\varepsilon^3)$. This means that using the incident velocity potential $\phi_0^{(3)}$ does not increase the order of accuracy any further. Therefore, it is sufficient to use the incident velocity potentials $\phi_0^{(1)}$ and $\phi_0^{(2)}$ of the NLS to compute the nonlinear FSI up to a modeling error of order $O(\varepsilon^3)$, i.e. an accuracy of order $O(\varepsilon^2)$.

Summary of the computation of the nonlinear FSI using the NLS

Using the NLS, the corresponding nonlinear FSI can be computed up to an error of order $O(\varepsilon^3)$. Here, the total velocity potential $\phi = \phi_0 + \phi_B$ is calculated considering its first- and second-order components, i. e.

$$\phi = \phi_0 + \phi_B = \varepsilon(\phi_0^{(1)} + \phi_B^{(1)}) + \varepsilon^2(\phi_0^{(2)} + \phi_B^{(2)}). \tag{30}$$

The incident velocity potentials $\phi_0^{(1)}$ and $\phi_0^{(2)}$ are given in Eq. (25). The velocity potentials $\phi_B^{(1)}$ and $\phi_B^{(2)}$ corresponding to the body disturbance can be calculated using the equations summarized in Fig. 1. As $\phi_B^{(1)}$ and $\phi_B^{(2)}$ depend on the geometry of the considered mechanical structure, they can generally only computed numerically. In the next section, a numerical scheme is sketched to compute $\phi_B^{(1)}$ and $\phi_B^{(2)}$ numerically. After computing the velocity potential $\phi = \phi_0 + \phi_B$, the hydrodynamic forces acting on a floating structure and the resulting motion of the structure can be calculated.

It has to be noted that the incident velocity potentials $\phi_0^{(1)}$ and $\phi_0^{(2)}$ are calculated using the wave envelope ψ, which satisfies the NLS (12). Since the NLS is accurate to the third order in the wave steepness, the NLS also accounts for corresponding nonlinear wave effects. For example, the NLS recovers the nonlinear dispersion relation, see Section 3.3.1. Therefore, the NLS can be used to compute the dynamics of the incident nonlinear water waves with a modeling error of order $O(\varepsilon^4)$. However, as shown, the corresponding nonlinear FSI is computed with a modeling error of order $O(\varepsilon^3)$.

Two different approaches for calculating the incident velocity potentials $\phi_0^{(i)}$ have been discussed so far: the first approach is based on Stokes waves, see Section 2.4, the second approach is based on the NLS (12). Both approaches have different advantages and disadvantages. Table 1 lists the PDEs and BCs that are satisfied by the corresponding incident velocity potentials $\phi_0^{(i)}$, and summarizes the properties of both approaches. Again, it is presented that the computational method, which uses the NLS, computes the corresponding FSI accurately only up to a modeling error of order $O(\varepsilon^3)$. However, advantages of the NLS-based approach include an efficient computation of incident velocity potentials $\phi_0^{(1)}$ and $\phi_0^{(2)}$, as the NLS has several known analytical solutions and can be numerically solved very efficiently using, for example, the ReSP scheme used in (Antoine and Duboscq, 2015; Hollm et al., 2024). Moreover, nonlinear wave-wave interactions are inherently accounted for by the NLS. This is not the case for the approach using Stokes waves, where nonlinear wave-wave interactions must be explicitly calculated to consider random nonlinear water waves. Thus, the NLS provides a promising framework for an efficient computation of the nonlinear FSI. This is especially the case when considering random water waves, which can be modeled using the NLS with the perturbation approach presented in Section 3.4.

5. Numerical scheme

In this paper, the advantages and limitations of using the NLS to compute the FSI are investigated. For this purpose, this section presents a numerical scheme to calculate the FSI between nonlinear water waves and a given mechanical structure. This includes the numerical calculation of the body disturbance potential ϕ_B, the hydrodynamic forces acting on the structure, and the resulting motion of the structure. Since cylinder elements are common constructional parts in offshore structures, this section presents a numerical scheme to compute the FSI between one cylindrical floating body (CFB) and water waves. The CFB is used here as an application example to show the potential of the computational method presented in Section 4.

5.1. Mechanical structure

Int this section, the CFB is introduced whose dynamics in linear and nonlinear waves will be studied in the rest of this work. Here, a CFB is considered, which moves along a guidance in the vertical direction. This example is taken from point-absorber wave energy converters, see e.g. (Yeung et al., 2012; Hollm et al., 2022b). Fig. 4 shows a sketch of the mechanical system in the $x - z$-plane. The CFB has a radius of R and a draft of D. The displacement of the CFB against its resting position is denoted by ξ. A semicircular bottom is used to prevent numerical difficulties, which would occur in the numerical discretization of the water domain around a sharp corner. Here, the sharp corners at the bottom of the cylinder are replaced by a spherical segment of radius R_S.

5.2. Computational domain and absorbing boundary conditions

In the following, the computational domain is specified, for which the velocity potential ϕ_B corresponding to the body disturbance of the CFB is computed numerically. Since the CFB shown in Fig. 4 is rotationally symmetric, the spatial computational domain is not only considered in Cartesian coordinates $(x, y, z) \in \mathbb{R}^3$ but also in cylindrical coordinates

Table 1
Comparison of the two presented approaches for the computation of the incident velocity potentials $\phi_0^{(i)}$.

Properties	Use incident potentials $\phi_0^{(i)}$ $(i = 1, 2)$ of Stokes waves presented in Section 2.4	Use incident potentials $\phi_0^{(i)}$ $(i = 1, 2)$ from NLS using Eq. (25)
$\nabla^2\phi_0^{(i)} = 0$?	Fulfilled	Fulfilled
$\phi_{0,z}^{(i)} = 0$ at $z = -h$?	Fulfilled	Not fulfilled, error decreases exponentially in h
$\phi_{0,tt}^{(1)} + g\phi_{0,z}^{(1)} = 0$ at $z = 0$?	Fulfilled	Not fulfilled, error of order $O(\varepsilon^2)$
$\phi_{0,tt}^{(2)} + g\phi_{0,z}^{(2)} = F(\phi_0^{(1)})$ at $z = 0$?	Fulfilled	Not fulfilled, error of order $O(\varepsilon^2)$
Advantages	• All PDEs and BCs are exactly fulfilled	• Straightforward and efficient computation • Nonlinear wave-wave interactions are directly considered • Nonlinear wave effects from the use of a third-order wave theory are taken into account
Disadvantages	• Interactions between water waves have to be explicitly considered in the irregular case • Computation of nonlinear wave-wave interactions is very time-consuming • Nonlinear wave effects from the use of a third-order wave theory are not considered	• All PDEs and BCs are only fulfilled up to a small error

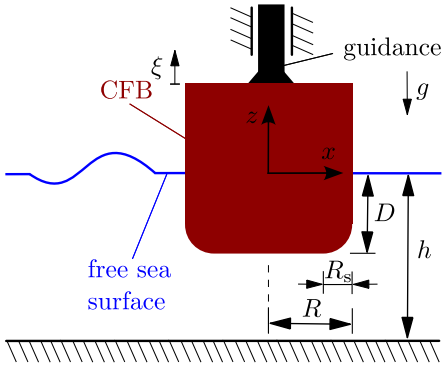

Fig. 4. Sketch of the considered CFB.

$(r, \theta, z) \in \mathbb{R}_+ \times (0, 2\pi] \times \mathbb{R}$. Here, $\mathbb{R}_+$ is defined as $\mathbb{R}_+ := \{x \in \mathbb{R} \mid x \geq 0\}$. The origins of the cylindrical and Cartesian coordinate systems are both located in the geometric center of the CFB at the height of the still water level, see Fig. 4. The set of all points, which are located inside the CFB and below the still water line at $z = 0$, is denoted by C_3. Since the CFB is moving in vertical direction, the boundary of C_3 changes in time.

For the numerical computation of the velocity potential ϕ_B, the computational water domain will be bounded in r-direction by some arbitrary value $R_\Omega \in \mathbb{R}_+$. Let Ω_3 denote the computational water domain. Then it holds

$$\Omega_3 := \{(r, \theta, z) \in \mathbb{R}^3 \setminus C_3 \mid 0 \leq r \leq R_\Omega,\ 0 < \theta \leq 2\pi,\ -h \leq z \leq 0\}. \tag{31}$$

To avoid unphysical wave reflections at the artificial outer boundary $r = R_\Omega$, absorbing BCs are implemented via the sponge layer method, which has been used, for example, in (Büchmann et al., 1998; Skourup et al., 2000; Shao and Faltinsen, 2013). Artificial damping is introduced by adding dissipative terms in the BC at $z = 0$ in a limited zone that is far away from the considered structure. The nature of the dissipative terms, which are added to the BC at $z = 0$, is arbitrary. In this work, the dissipative terms depend on the sea surface displacement η and velocity potential ϕ, respectively. They are introduced by reformulating the BCs (1b) and (1c) to

$$\eta_t + \phi_x\eta_x + \phi_y\eta_y + \mu(x, y)\eta = \phi_z, \qquad \text{for } R \leq r \leq R_\Omega,\ z = \eta(x, y, t), \tag{32a}$$

$$\phi_t + \frac{1}{2}\nabla\phi \cdot \nabla\phi + g\eta + \mu(x, y)\phi = 0, \qquad \text{for } R \leq r \leq R_\Omega,\ z = \eta(x, y, t). \tag{32b}$$

A similar approach for introducing the dissipative terms has been used several times in literature, see e.g. (Büchmann et al., 1998; Skourup et al., 2000; Shao and Faltinsen, 2013).

Starting with Eq. (32) and following the same procedure as has been presented in Section 2.2 and Section 2.3, it is found that the velocity potentials $\phi_B^{(1)}$ and $\phi_B^{(2)}$ can be computed in the presence of the damping μ by solving

$$\nabla^2\phi_B^{(i)} = 0, \qquad \text{in } \mathring{\Omega}_3, \tag{33a}$$

$$\nabla\phi_B^{(i)} \cdot \mathbf{n} = -\nabla\phi_0^{(i)} \cdot \mathbf{n} + \mathbf{u}^{(i)} \cdot \mathbf{n}, \quad \text{on } \partial C_3, \tag{33b}$$

$$\phi_{B,z}^{(i)} = 0, \qquad \text{on } \partial\Omega_3 \cap \{z = -h\}, \tag{33c}$$

$$\phi_{B,tt}^{(i)} + g\phi_{B,z}^{(i)} + 2\mu\phi_{B,t}^{(i)} + \mu^2\phi_B^{(i)} = G^{(i)}(\phi_0^{(1)}, \phi_B^{(1)}), \quad \text{on } \partial\Omega_3 \cap \{z = 0\}, \tag{33d}$$

$$\nabla\phi_B^{(i)} \cdot \mathbf{n} = 0, \qquad \text{on } \partial\Omega_3 \cap \{r = R_\Omega\}, \tag{33e}$$

whereby $G^{(1)} = 0$, $G^{(2)} = F^\mu(\phi_0^{(1)} + \phi_B^{(1)}) - F^\mu(\phi_0^{(1)})$, and

$$\begin{aligned} F^\mu(\phi^{(1)}) = &- 2\nabla\phi^{(1)} \cdot \nabla\phi_t^{(1)} - \frac{3}{2}\mu\nabla\phi^{(1)} \cdot \nabla\phi^{(1)} - \phi^{(1)}\left(\nabla\phi^{(1)} \cdot \nabla\mu\right) \\ &+ \frac{1}{g}\left[\phi_t^{(1)} + \mu\phi^{(1)}\right]\frac{\partial}{\partial z}\left(\phi_{tt}^{(1)} + g\phi_z^{(1)} + 2\mu\phi_t^{(1)} + \mu^2\phi^{(1)}\right). \end{aligned} \tag{34}$$

Furthermore, $\mathring{\Omega}_3$ denotes the interior of the set Ω_3, $\partial\Omega_3$ the boundary of Ω_3, and ∂C_3 the boundary of C_3. Note that reflecting Neumann BCs are assumed at $r = R_\Omega$. In this way, water waves lose energy if they pass through the damping zone on their way out of the domain and then, for the part that is reflected at $r = R_\Omega$, on their way back. For $\mu = 0$, Eqs. (33a)-(33d) reduce to the same equations as summarized in Fig. 1.

Note that the damping μ is only active in a damping zone far away from the structure. In this work, the same value for μ is used as in (Shao and Faltinsen, 2013). This damping is given in terms of the cylindrical coordinate r by

$$\mu(r) := \begin{cases} 0, \text{ for } 0 \leq r < R_i, \\ -\frac{g\ln(0.5\times10^{-5})}{2\omega L}\left[-2\left(\frac{r-R_i}{L}\right)^3 + 3\left(\frac{r-R_i}{L}\right)^2\right], \text{ for } R_i \leq r \leq R_\Omega. \end{cases} \tag{35}$$

Here, R_i is the radius of an inner layer, where no damping is considered. Furthermore, ω is the wave frequency of the incoming water waves. In (Shao and Faltinsen, 2013), the length $L = R_\Omega - R_i$ of the damping zone has been chosen to be twice as large as the wavelength of the incoming waves.

5.3. Transformation of governing equations

Before a numerical scheme to solve Eq. (33) is presented, it is shown how the computational effort can be reduced by transforming Eq. (33) from one three-dimensional problem to multiple uncoupled two-dimensional problems. This is done in three steps.

5.3.1. Step 1: Transformation to the resting position

Since the CFB is moving, the domains C_3 and Ω_3 change in time. In order to simplify the study, the resting position of the CFB is considered in the numerical computation of $\phi_\mathrm{B}^{(i)}$ for the whole computation time. Let $\bar{C}_3$ be the domain C_3 for the case that the CFB is located at its resting position. When the CFB is considered in its resting position, the corresponding BC (33b) at the surface of the CFB has to be transformed from ∂C_3 to $\partial\bar{C}_3$. This is done by following the method presented in (Ogilvie, 1983). It is found that the resulting BC at $\partial\bar{C}_3$ is given by

$$\nabla\phi_\mathrm{B}^{(i)}\cdot\mathbf{n} = -\nabla\phi_0^{(i)}\cdot\mathbf{n} + \mathbf{u}^{(i)}\cdot\mathbf{n} + V^{(i)}(\phi_0^{(1)},\phi_\mathrm{B}^{(1)},\xi^{(1)}), \quad \text{on } \partial\bar{C}_3, \tag{36}$$

whereby $V^{(1)}=0$, and $V^{(2)} = -\xi^{(1)}\dfrac{\partial}{\partial z}\nabla(\phi_0^{(1)}+\phi_\mathrm{B}^{(1)})\cdot\mathbf{n}$.

Here, it is assumed that the displacement ξ of the CFB in the vertical direction can be expanded in a similar perturbation expansion as has been presented in Eq. (4) for the velocity potential ϕ, i.e. $\xi = \varepsilon\,\xi^{(1)} + \varepsilon^2\xi^{(2)} + O(\varepsilon^3)$. It should be noted that the change from ∂C_3 to $\partial\bar{C}_3$ also changes the computational water domain in Eq. (33) from Ω_3 to

$$\bar{\Omega}_3 := \{(r,\theta,z)\in\mathbb{R}^3\setminus\bar{C}_3 \mid 0\le r\le R_\Omega,\ 0<\theta\le 2\pi,\ -h\le z\le 0\}. \tag{37}$$

5.3.2. Step 2: Consideration of equations in cylindrical coordinates

In the second step, the Eqs. (33) and (36) are considered in cylindrical coordinates. This is done by considering the velocity potentials $\phi_\mathrm{B}^{(i)}$ and $\phi_0^{(i)}$ in cylindrical coordinates (r,θ,z). When considering the BC (36) in cylindrical coordinates, it has to be noted that a normal vector $\mathbf{n}$ pointing out of the fluid and inside the rotationally symmetric floating body has, in cylindrical coordinates, the form

$$\mathbf{n} = \begin{bmatrix} n^r \\ 0 \\ n^z \end{bmatrix}, \quad \text{with } n^r\le 0, n^z\ge 0, \text{ and } \sqrt{(n^r)^2+(n^z)^2} = 1. \tag{38}$$

5.3.3. Step 3: Application of Fourier transform

Finally, in step 3, the velocity potential $\phi_\mathrm{B}^{(i)}(r,\theta,z,t)$ is approximated by a Fourier series expansion. Since $\phi_\mathrm{B}^{(i)}$ is periodic in θ, it can be approximated by a truncated Fourier series of the form

$$\phi_\mathrm{B}^{(i)}(r,\theta,z,t) = \sum_{m=-N_\mathrm{F}/2}^{N_\mathrm{F}/2-1} \widehat{\phi}_{\mathrm{B},m}^{(i)}(r,z,t)\mathrm{e}^{\mathrm{i}m\theta}. \tag{39}$$

Here, the complex Fourier coefficients $\widehat{\phi}_{\mathrm{B},m}^{(i)}$ are given by

$$\widehat{\phi}_{\mathrm{B},m}^{(i)}(r,z,t) = \frac{1}{N_\mathrm{F}}\sum_{j=0}^{N_\mathrm{F}-1}\phi_\mathrm{B}^{(i)}(r,\theta_j,z,t)\mathrm{e}^{-\mathrm{i}m\theta_j}, \tag{40}$$

whereby $\theta_j = 2j\pi/N_\mathrm{F}$ and N_F is the number of grid points along a circle. Substituting Eq. (39) into the corresponding equations for $\phi_\mathrm{B}^{(i)}$ derived in step 2 shows that the Fourier coefficients $\widehat{\phi}_{\mathrm{B},m}^{(i)}$, $m=-\frac{N_\mathrm{F}}{2},\dots,\frac{N_\mathrm{F}}{2}-1$, have to satisfy

$$\widehat{\phi}_{\mathrm{B},m,rr}^{(i)} + \frac{\widehat{\phi}_{\mathrm{B},m,r}^{(i)}}{r} - \frac{m^2}{r^2}\widehat{\phi}_{\mathrm{B},m}^{(i)} + \widehat{\phi}_{\mathrm{B},m,zz}^{(i)} = 0, \quad \text{in } \mathring{\bar{\Omega}}_2, \tag{41a}$$

$$\widehat{\phi}_{\mathrm{B},m,r}^{(i)}n^r + \widehat{\phi}_{\mathrm{B},m,z}^{(i)}n^z = -\widehat{\phi}_{0,m,r}^{(i)}n^r - \widehat{\phi}_{0,m,z}^{(i)}n^z + u_3^{(i)}n^z\widehat{1}_m + \widehat{V}_m^{(i)}, \quad \text{on } \partial\bar{C}_2, \tag{41b}$$

$$\widehat{\phi}_{\mathrm{B},m,z}^{(i)} = 0, \quad \text{on } \partial\bar{\Omega}_2\cap\{z=-h\}, \tag{41c}$$

$$\widehat{\phi}_{\mathrm{B},m,tt}^{(i)} + g\,\widehat{\phi}_{\mathrm{B},m,z}^{(i)} + 2\mu\,\widehat{\phi}_{\mathrm{B},m,t}^{(i)} + \mu^2\,\widehat{\phi}_{\mathrm{B},m}^{(i)} = \widehat{G}_m^{(i)}, \quad \text{on } \partial\bar{\Omega}_2\cap\{z=0\}, \tag{41d}$$

$$\widehat{\phi}_{\mathrm{B},m,r}^{(i)} = 0, \quad \text{on } \partial\bar{\Omega}_2\cap\{r=R_\Omega\}. \tag{41e}$$

Here, the sets $\bar{\Omega}_2$ and $\bar{C}_2$ are defined by

$$\bar{\Omega}_2 := \{(r,z)\in\mathbb{R}^2 \mid (r,\theta,z)\in\bar{\Omega}_3,\ 0<\theta\le 2\pi\}, \text{ and} \tag{42a}$$

$$\bar{C}_2 := \{(r,z)\in\mathbb{R}^2 \mid (r,\theta,z)\in\bar{C}_3,\ 0<\theta\le 2\pi\}. \tag{42b}$$

Furthermore, the respective m-th Fourier coefficient of the incident velocity potential $\widehat{\phi}_{0,m}$ and the right-hand side functions $\widehat{G}_m^{(i)}$ and $\widehat{V}_m^{(i)}$ is defined similarly to Eq. (39). Furthermore, $\widehat{1}_m$ is the m-th Fourier coefficient of the constant function $f(r,\theta,z)=1$.

In this way, the calculation of the velocity potentials $\phi_\mathrm{B}^{(i)}$ in a three-dimensional spatial domain has been replaced by N_F decoupled two-dimensional problems in which the corresponding Fourier coefficients $\widehat{\phi}_{\mathrm{B},m}^{(i)}$ are calculated.

5.4. Numerical computation of the body disturbance velocity potential ϕ_B

In order to compute the Fourier coefficients $\widehat{\phi}_{\mathrm{B},m}^{(1)}$ and $\widehat{\phi}_{\mathrm{B},m}^{(2)}$, Eq. (41) is solved using a finite difference scheme. The corresponding temporal and spatial grids as well as the used finite difference discretizations of Eq. (41) are given in Appendix C.

After computing the Fourier coefficients $\widehat{\phi}_{\mathrm{B},m}^{(1)}$ and $\widehat{\phi}_{\mathrm{B},m}^{(2)}$, $m=-\frac{N_\mathrm{F}}{2},\dots,\frac{N_\mathrm{F}}{2}-1$, the velocity potentials $\phi_\mathrm{B}^{(1)}$ and $\phi_\mathrm{B}^{(2)}$ can be calculated using Eq. (39). Adding $\phi_\mathrm{B}^{(1)}$ and $\phi_\mathrm{B}^{(2)}$ to the incident velocity potentials $\phi_0^{(1)}$ and $\phi_0^{(2)}$ yields the velocity potentials $\phi^{(1)}$ and $\phi^{(2)}$, which are the Stokes components of the total velocity potential ϕ, see Eq. (9). With $\phi^{(1)}$, $\phi^{(2)}$, and ϕ, the velocity potentials are determined that correspond to the water waves, which are disturbed by the presence and motion of the CFB.

5.5. Hydrodynamic forces and equation of motion

In the following, formulas for the hydrodynamic forces acting on the CFB and the resulting motion of the CFB are presented. The acting hydrodynamic torques are not considered here, as the CFB shown in Fig. 4 can only perform translational motion in the vertical direction.

The hydrodynamic forces acting on a general mechanical structure are calculated by integrating the hydrodynamic pressure p over the wetted surface S_B of the structure. Here, the hydrodynamic pressure p can be computed by means of Bernoulli's equation, whereby $p=p(\phi)$ depends on the velocity potential $\phi=\phi_0+\phi_\mathrm{B}$. Based on the Stokes expansion $\phi=\varepsilon\phi^{(1)}+\varepsilon^2\phi^{(2)}$, the hydrodynamic forces acting on the CFB are given by

$$\mathbf{F} = \iint_{S_\mathrm{B}} p\mathbf{n}\,\mathrm{d}S = \mathbf{F}^{(0)} + \varepsilon^1\mathbf{F}^{(1)} + \varepsilon^2\mathbf{F}^{(2)} + O(\varepsilon^3), \tag{43}$$

with

$$\begin{aligned} \mathbf{F}^{(0)} &= -\iint_{\partial C_3}\rho g z\mathbf{n}\,\mathrm{d}S, \qquad \mathbf{F}^{(1)} = -\iint_{\partial C_3}\rho\phi_t^{(1)}\mathbf{n}\,\mathrm{d}S, \\ \mathbf{F}^{(2)} &= -\iint_{\partial C_3}\left(\rho\phi_t^{(2)} + \rho\frac{1}{2}\nabla\phi^{(1)}\cdot\nabla\phi^{(1)}\right)\mathbf{n}\,\mathrm{d}S + \int_{\bar{C}_0}\frac{1}{2}\rho g\left(\eta^{(1)}\right)^2\mathbf{n}\,\mathrm{d}C, \end{aligned} \tag{44}$$

see e.g. (Eatock Taylor and Hung, 1987). Recall that ∂C_3 denotes the surface of the part of the CFB, which is located below the still water line at $z=0$. Furthermore, ρ denotes the water density and C_0 the cross-section of ∂C_3 and $z=0$.

Note that all surface integrands appearing in Eq. (43) are integrated over the surface ∂C_3, which changes in time with the moving CFB. However, the velocity potentials $\phi_\mathrm{B}^{(i)}$ have only been computed for the CFB in its resting position, see Section 5.3.1. To compute the forces $\mathbf{F}^{(1)}$ and $\mathbf{F}^{(2)}$, the corresponding integrals are therefore transformed from ∂C_3 to $\partial\bar{C}_3$ using the formulas and results presented in (Ogilvie, 1983). For the CFB considered in this work, which can perform translational motion in the vertical direction with displacement $\xi=\varepsilon\,\xi^{(1)}+\varepsilon^2\xi^{(2)}+O(\varepsilon^3)$, the

forces $\mathbf{F}^{(1)}$ and $\mathbf{F}^{(2)}$ become

$$\begin{aligned}\mathbf{F}^{(1)} &= -\iint_{\partial\bar{C}_3} \rho\phi_t^{(1)}\mathbf{n}\,\mathrm{d}S,\\ \mathbf{F}^{(2)} &= -\iint_{\partial\bar{C}_3} \left(\rho\phi_t^{(2)} + \rho\frac{1}{2}\nabla\phi^{(1)}\cdot\nabla\phi^{(1)} + \rho\,\xi^{(1)}\phi_{tz}^{(1)}\right)\mathbf{n}\,\mathrm{d}S\\ &\quad + \int_{\bar{C}_0} \frac{1}{2}\rho g\left(\eta^{(1)}-\xi^{(1)}\right)^2\mathbf{n}\,\mathrm{d}C.\end{aligned} \tag{45}$$

Since $\mathbf{F}^{(0)}$ does not depend on any velocity potential, it is possible to directly compute $\mathbf{F}^{(0)}$ without any transformation of the corresponding integral.

After calculating the nonlinear hydrodynamic forces acting on the CFB by numerical integration, the equation of motion of the CFB can be formulated. Let the respective component of the force $\mathbf{F}^{(i)}$ in the x-, y-, and z-direction be denoted by $F_1^{(i)}$, $F_2^{(i)}$, and $F_3^{(i)}$, respectively, i. e. $\mathbf{F}^{(i)} = [F_1^{(i)}, F_2^{(i)}, F_3^{(i)}]^{\mathrm{T}}$. Following Hollm and Seifried (2023), the corresponding equations of motion for $\xi^{(1)}$ and $\xi^{(2)}$ are given by

$$m\ddot{\xi}^{(1)} + d\dot{\xi}^{(1)} + \rho g\pi R^2\xi^{(1)} = F_3^{(1)}, \quad m\ddot{\xi}^{(2)} + d\dot{\xi}^{(2)} + \rho g\pi R^2\xi^{(2)} = F_3^{(2)}. \tag{46}$$

Here, m is the combined mass of the CFB and the guidance. Furthermore, d is a constant that accounts for the total velocity-dependent damping force from mechanical friction effects and viscous damping in the z-direction (Hollm et al., 2022b). In this work, Eq. (46) is always solved using the fourth-order Adams-Bashforth-Moulton predictor-corrector scheme. After computing $\xi^{(1)}$ and $\xi^{(2)}$, the total displacement ξ of the CFB can be computed.

Note that this section has presented a numerical scheme to compute the FSI with a CFB, which can only perform translational vertical motion. However, the presented numerical scheme can also be extended to structures that can perform general three-dimensional motion by modifying the Eqs. (36), (45), and (46) accordingly. As the advantages and limitations of using the NLS to calculate the FSI between mechanical structures and random nonlinear water waves are discussed in this work, the considered CFB is used as an application example in the following.

6. Validation of numerical results

In the previous section, a numerical scheme to compute the velocity potentials $\phi_{\mathrm{B}}^{(i)}$, hydrodynamic forces $\mathbf{F}^{(i)}$ acting on the considered CFB, and the resulting displacements $\xi^{(i)}$ of the CFB, $i = 1, 2$, has been presented. In this section, the numerical solution of the resulting FSI simulation is validated by comparing the corresponding results with those presented in literature.

6.1. Validation of first-order terms

The considered CFB starts to move from its resting position, but only steady-state results are considered. The used system and damping parameters of the CFB are given by $R = 1\,\mathrm{m}$, $R_{\mathrm{S}} = 0\,\mathrm{m}$, $D = 1.5\,\mathrm{m}$ and $d = 3000\,\frac{\mathrm{kg}}{\mathrm{s}}$. Furthermore, the corresponding water density and depth are set to $\rho = 1023\,\frac{\mathrm{kg}}{\mathrm{m}^3}$ and $h = 4\,\mathrm{m}$.

In the following, the CFB shown in Fig. 4 is excited by regular Stokes waves of first and second order, where the corresponding velocity potentials are given by Eq. (10) with $\omega = 1\,\frac{\mathrm{rad}}{\mathrm{s}}$, $A = 0.4\,\mathrm{m}$, and $\chi = 0$. The respective wavelength λ is given by $\lambda = 36.673\,\mathrm{m}$. Simulations run for $t \in [0, 50\,\mathrm{s}]$ using the numerical scheme presented in Section 5 with the step sizes $\Delta r = \Delta z = 0.04\,\mathrm{m}$ and $\Delta t = 0.05\,\mathrm{s}$. Here, absorbing BCs are implemented using the damping μ from Eq. (35) with $R_{\mathrm{i}} = \lambda$ and $L = 2\lambda$.

The velocity potentials $\phi_{\mathrm{B}}^{(i)}$, $i = 1, 2$, are computed using Fourier series expansions with $N_{\mathrm{F}} = 16$ Fourier coefficients. Further investigations have shown that larger values for N_{F} do not change the numerical results significantly for the considered system parameters.

Fig. 5a-b presents the hydrodynamic forces acting on the CFB in the x- and z-direction. The corresponding displacement of the CFB is shown in Fig. 5c. Here, the first- and second-order components of the forces and displacement are presented. Also the total results up to second order are shown. To present these results in a better way, Fig. 6 shows snapshots that illustrate the motions of the incoming regular water waves and the CFB at four different timepoints over a single wave-cycle. The corresponding results following from the use of a linear and nonlinear FSI are presented, respectively. Here, the presented incoming regular water waves are given by $\eta = \varepsilon\eta^{(1)} = A\cos(kx - \omega t)$ in the linear and $\eta = \varepsilon\eta^{(1)} + \varepsilon^2\eta^{(2)}$ in the nonlinear case. The position of the CFB is presented with displacement $\xi = \varepsilon\xi^{(1)}$ in the linear and $\xi = \varepsilon\xi^{(1)} + \varepsilon^2\xi^{(2)}$ in the nonlinear case.

Considering Fig. 5, it can be seen that all first-order components oscillate in time with frequency ω, while the second-order components oscillate in time with frequency 2ω. This directly follows from the fact that the first- and second-order incoming velocity potentials $\phi_0^{(1)}$ and $\phi_0^{(2)}$ from Eq. (10) oscillate in time with frequencies ω and 2ω, respectively.

Furthermore, it has to be noted that the amplitudes of the second-order results are relatively large compared to those of the corresponding first-order results. Therefore, the second-order components of the forces and displacement and cannot be neglected in the computation of the FSI for the considered water wave and structure.

In order to validate the numerical results for the first-order components of the motion and forces, Fig. 5 also show the corresponding results obtained using the linear method presented, for example, in (Hollm et al., 2022b). Here, for regular water waves, the motion of the CFB is described by

$$(M + \mu_{3,3})\ddot{\xi} + (\lambda_{3,3} + d)\dot{\xi} + \rho g\pi R^2\xi = \mathrm{Re}\{A f_3 \mathrm{e}^{-\mathrm{i}\omega t}\}. \tag{47}$$

The resulting hydrodynamic forces acting on the CFB in x- and z-direction are given by $F_1 = \mathrm{Re}\{A f_1 \mathrm{e}^{-\mathrm{i}\omega t}\}$ and $F_3 = \mathrm{Re}\{A f_3 \mathrm{e}^{-\mathrm{i}\omega t}\} - \mu_{3,3}\ddot{\xi} - \lambda_{3,3}\dot{\xi}$. Hydrodynamic forces resulting from diffraction and radiation effects are considered here. For a cylindrical body, the hydrodynamic coefficients f_1, f_3, $\mu_{3,3}$, and $\lambda_{3,3}$ can be computed semi-analytically using the methods presented in (Yeung, 1981) and (Garrett, 1971).

It can be seen that the numerical results for the first-order components of the motion and hydrodynamic forces, which have been computed using the numerical scheme presented in Section 5 and the linear method presented in (Hollm et al., 2022b), agree very well with each other. The relative errors between the corresponding results on force and displacements are all between 0.1 % and 0.22 %. This validates the results of the first-order components of the displacement and hydrodynamic forces.

6.2. Validation of second-order terms

In order to validate the results of the corresponding second-order components, numerical results are compared with the semi-analytical results presented in (Kinoshita and Bao, 2000). Here, the authors investigate the forces acting on a fixed cylinder for different system parameters and incoming regular Stokes waves. For example, the amplitudes of the second-order hydrodynamic forces $\varepsilon^2 F_1^{(2)}$ and $\varepsilon^2 F_3^{(2)}$ are studied for incoming regular Stokes waves with a varying wave number k. The results, which are computed using the numerical scheme presented in Section 5, are shown in Fig. 7. The forces are normalized according to (Kinoshita and Bao, 2000). A CFB is considered with radius $R = 1\,\mathrm{m}$, $R_{\mathrm{S}} = 0$, and draft $D = 4\,\mathrm{m}$, which is positioned in water of depth $h = 10\,\mathrm{m}$. The amplitude of the incoming regular Stokes waves is $A = 0.15\,\mathrm{m}$. Fig. 7 also shows the corresponding results presented in (Kinoshita and Bao, 2000, Fig. 5). It can be seen that both results agree very well with each other. Further investigations have shown that also other results presented in (Kinoshita and Bao, 2000) can be regenerated very well by the numerical scheme presented in Section 5.

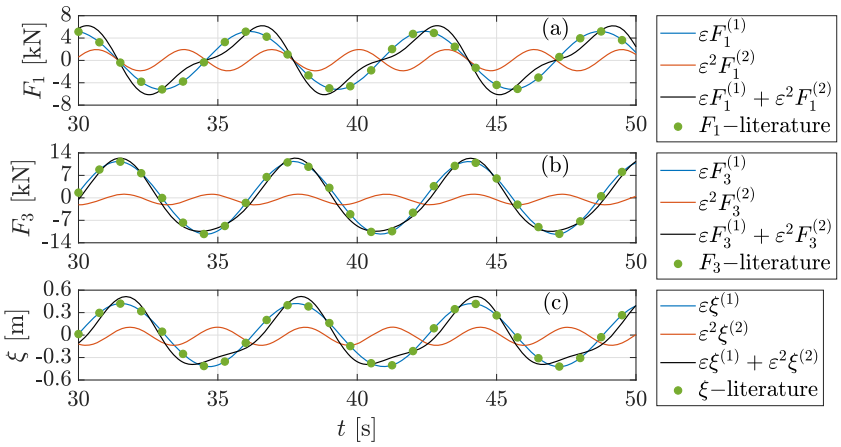

Fig. 5. Forces in (a) x-direction and (b) z-direction, which act on the CFB in regular Stokes waves of first and second order. (c) Displacement of the CFB in regular Stokes waves of first and second order. Furthermore, the corresponding results are shown, which result from the linear method presented, for example, in (Hollm et al., 2022b).

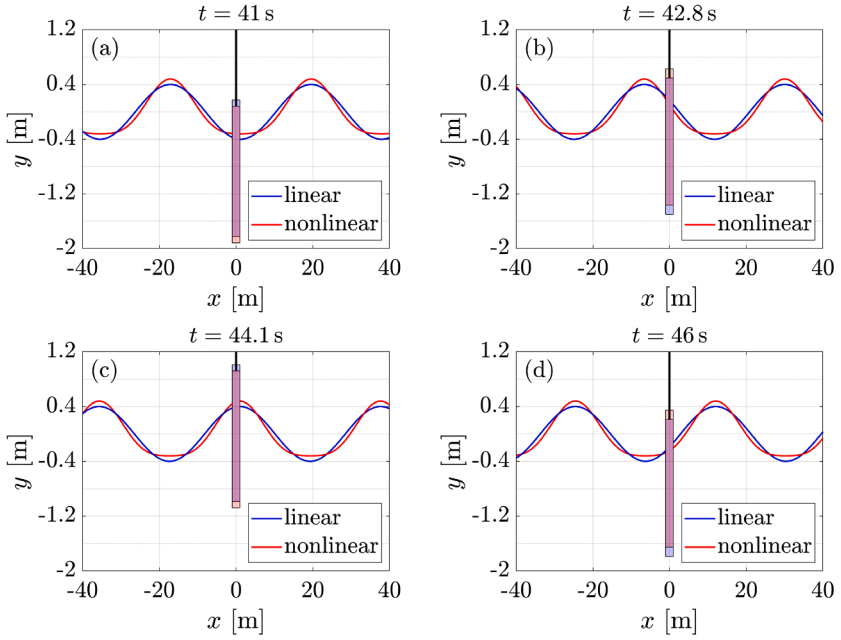

Fig. 6. Snapshots of the motions of the incoming regular water waves and the CFB at four different timepoints. The corresponding results following from the use of a linear and nonlinear FSI are presented, respectively.

Therefore, all numerical results presented in this section, which are obtained using the method presented in Section 5, are validated by corresponding results taken from literature. Further investigations have also revealed that the numerical approximations for the unknown hydrodynamic forces and motion of the CFB are converging with order two in the spatial and temporal stepsizes Δr, Δz, and Δt, respectively. For details, see (Hollm, 2025). This finishes the validation of the numerical scheme presented in Section 5.

7. Dynamics of mechanical structures in nonlinear water waves

After having shown in Section 4 how the NLS can be used to compute the FSI with a mechanical structure, a numerical scheme has been presented and validated in Sections 5 and 6 to compute FSI results. In this section, further simulation results for the FSI are presented. Specifically, the FSI between the CFB shown in Fig. 4 and incoming water waves corresponding to the NLS is analyzed. In all investigations, the CFB starts moving from its resting position. However, only the results obtained in the steady state are considered. The used system and damping parameters of the CFB are given by $R = 1\,\mathrm{m}$, $R_S = 0.2\,\mathrm{m}$, $D = 1.5\,\mathrm{m}$ and $d = 3000\,\frac{\mathrm{kg}}{\mathrm{s}}$. Furthermore, the CFB is moving in salt water with density $\rho = 1023\,\frac{\mathrm{kg}}{\mathrm{m}^3}$. Only long-crested water waves are considered, which propagate in the x-direction.

In the following, the FSI between the CFB and water waves corresponding to the plane-wave and Peregrine breather solution of the NLS is investigated. First, regular water waves are considered in Section 7.1 using the plane-wave solution of the NLS. Corresponding FSI results are compared with those, where regular waves are described using Stokes waves. Afterward, the FSI between the CFB and the analytical Peregrine breather solution of the NLS is investigated in Section 7.2. In Section 7.3, it is investigated how the FSI results from Section 7.2 change if the Peregrine breather solution is initially perturbed by an irregular sea state. Finally, this section concludes with a discussion of the presented results in Section 7.4.

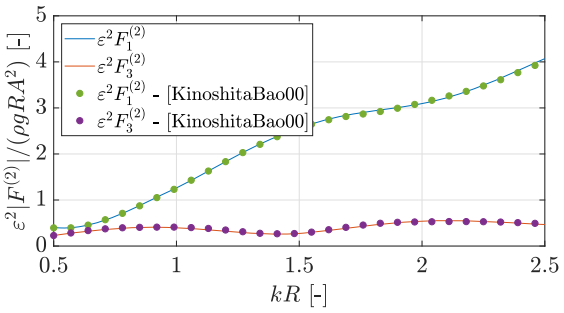

Fig. 7. Amplitudes of the second-order hydrodynamic forces acting in the horizontal and vertical direction against a varying wave number k. The numerical results are compared with those presented in (Kinoshita and Bao, 2000, Fig. 5).

7.1. Analysis of FSI in regular waves

The plane-wave solution of the NLS (12) is given by Eq. (21) and can be used to describe regular water waves, which fulfill the nonlinear dispersion relation, see Section 3.3.1. However, regular water waves can also be described using Stokes waves, see Section 2.4.

In this section, it is studied whether the use of regular Stokes waves and the plane-wave solution of the NLS leads to the same results for the FSI. Here, the incident velocity potentials $\phi_0^{(1)}$ and $\phi_0^{(2)}$ of the Stokes waves are computed using Eq. (10). Waves are considered with amplitude $A = 0.2\,\mathrm{m}$, wave number $k = 0.5\,\mathrm{m}^{-1}$ and wavelength $\lambda = 4\pi$ in a sea with depth $h = 7\,\mathrm{m}$. Using these parameters, the resulting waves have a steepness of $Ak = 0.1$. Furthermore, the deep water condition is fulfilled, i. e. $h \geq \frac{1}{2}\lambda = 2\pi$. The corresponding wave frequency $\omega = \omega_{\mathrm{st}}$ of the Stokes waves can be calculated using the linear dispersion relation, i. e. $\omega_{\mathrm{st}} = \sqrt{kg\tanh(kh)} = 2.2127\,\frac{\mathrm{rad}}{\mathrm{s}}$.

When considering the plane-wave solution of the NLS, the corresponding wave envelope ψ is computed using Eq. (21) with $\psi_0 = 2\,\mathrm{m}$, $k_0 = 0.5\,\mathrm{m}^{-1}$, and $\varepsilon = 0.1$. The corresponding carrier wave frequency ω_0 is given by $\omega_0 = \sqrt{k_0 g} = 2.2147\,\frac{\mathrm{rad}}{\mathrm{s}}$. Since h fulfills the deep water condition, it holds $\tanh(kh) \approx 1$ and $\omega_0 \approx \omega_{\mathrm{st}}$. The corresponding incident velocity potentials $\phi_0^{(1)}$ and $\phi_0^{(2)}$ of the plane-wave solution of the NLS are calculated using Eq. (25).

All FSI results presented in this section are computed numerically using the numerical scheme presented in Section 5 with $N_{\mathrm{F}} = 16$ Fourier modes. Absorbing BCs are implemented using the damping μ from Eq. (35) with $R_{\mathrm{i}} = \lambda$ and $L = 2\lambda$. Corresponding numerical results for the FSI are calculated using the step sizes $\Delta r = \Delta z = 0.04\,\mathrm{m}$ and $\Delta t = 0.05\,\mathrm{s}$.

In the following, the hydrodynamic forces acting on the CFB are investigated. Fig. 8 presents the forces, which result from the use of Stokes waves and the waves corresponding to the NLS, respectively. Here, the first- and second-order component of the force acting in the vertical direction are shown, i. e. , $\varepsilon F_3^{(1)}$ and $\varepsilon^2 F_3^{(2)}$. The system is considered in its steady state. To visualize the differences in the oscillation periods, the results for the hydrodynamic forces are shifted in time so that the forces have a maximum at $t = 0$.

It can be seen that the hydrodynamic forces differ slightly in their oscillation periods and heights. Compared to the regular Stokes waves, the use of the NLS results in forces $\varepsilon F_3^{(1)}$ and $\varepsilon^2 F_3^{(2)}$ with higher frequencies. The relative difference between the heights of the first-order force $\varepsilon F_3^{(1)}$ is 1.64 %, and for the second-order force $\varepsilon^2 F_3^{(2)}$, it is 2.95 %.

The difference in the oscillation periods results from the fact the considered Stokes waves include nonlinear wave effects up to second-order, while the NLS accounts for third-order nonlinearities. In particular, the plane-wave solution of the NLS satisfies the nonlinear dispersion relation from Eq. (22), whereas Stokes waves satisfy the linear dispersion relation. Consequently, waves corresponding to the plane-wave solution of the NLS oscillate in time with frequency $\omega_{\mathrm{NLS}} > \omega_0 \approx \omega_{\mathrm{st}}$, where ω_{NLS} depends on the wave amplitude and is given by Eq. (22).

Considering the different heights of the forces $\varepsilon F_3^{(1)}$ and $\varepsilon^2 F_3^{(2)}$, it has to be noted that the amplitude of the hydrodynamic forces acting on the CFB are frequency-dependent. However, there is the question whether the difference in the heights of the forces presented in Fig. 8 only results from the different frequencies of the incoming water waves. To answer this question, additional Stokes waves with frequency ω_{NLS} have been analyzed. When these Stokes waves are considered, the relative difference between the heights of hydrodynamic forces $F_3^{(1)}$ reduces from 1.64 % to 0.38 %, and for the second-order force $\varepsilon^2 F_3^{(2)}$, it reduces from 2.95 % to 0.23 %. These differences can be even further reduced by increasing the water depth h. Recall that the NLS is only valid for $h \to \infty$. Additional simulations have shown that increasing the water depth from $h = 7\,\mathrm{m}$ to $h = 10\,\mathrm{m}$ reduces the difference between the heights of the forces $\varepsilon F_3^{(1)}$ from 0.38 % to 0.04 %. For $\varepsilon^2 F_3^{(2)}$, the relative difference is reduced from 0.23 % to 0.01 %.

Therefore, it has been shown that the slightly different behaviors of the hydrodynamic forces presented in Fig. 4 arise from the different frequencies of the incoming water waves and the use of a too small water depth h. It follows that the use of the plane-wave solution of the NLS and regular Stokes waves yields equivalent FSI results. This validates the use of the NLS and the corresponding computational method presented in Section 4 for the calculation of the FSI with regular water waves in deep water.

7.2. Interaction with the analytical Peregrine breather solution

Next, the FSI between the CFB and water waves corresponding on the Peregrine breather solution of the NLS is studied. The wave envelope ψ of the Peregrine breather solution is calculated using Eq. (23) with parameters $k_0 = 0.5\,\mathrm{m}^{-1}$, $\psi_0 = 1.5\,\mathrm{m}$, $\varepsilon = 0.1$, and $X_{\mathrm{s}} = 44.29\,\mathrm{m}$. Fig. 2 shows the corresponding amplitude $|\psi|$ of the analytical solution.

The corresponding FSI results are computed numerically in water of depth $h = 7\,\mathrm{m}$ over the time interval $t \in [-200\,\mathrm{s}, 200\,\mathrm{s}]$. The same damping μ, domain $\bar{\Omega}$, and step sizes Δr, Δz, and Δt as in Section 7.1 are used. Moreover, the CFB is positioned at $x = X_{\mathrm{s}}/\varepsilon = 442.94\,\mathrm{m}$. In this way, the peak amplitude waves of the Peregrine breather solution reach the CFB at $t = 0\,\mathrm{s}$.

Fig. 9a shows the sea surface displacements $\varepsilon\eta_{\mathrm{inc}}^{(1)}$ and $\varepsilon^2\eta_{\mathrm{inc}}^{(2)}$ of the incoming water waves of first- and second-order. These are the waves that would be measured in the absence of the CFB at the location of the center of the CFB. Given the incident velocity potentials $\phi_0^{(1)}$ and $\phi_0^{(2)}$ from Eq. (25), $\eta_{\mathrm{inc}}^{(1)}$ and $\eta_{\mathrm{inc}}^{(2)}$ are calculated using Eq. (A.2a). The values of $\varepsilon\eta_{\mathrm{inc}}^{(1)}$ and $\varepsilon^2\eta_{\mathrm{inc}}^{(2)}$ are shown to better understand the corresponding results for the hydrodynamic forces acting on the CFB and the displacement of the CFB.

The corresponding first- and second-order components of the hydrodynamic forces acting on the CFB in the horizontal and vertical directions, $F_1^{(i)}$ and $F_3^{(i)}$, $i = 1, 2$, are presented in Figs. 9b and 9c. These forces are computed using the velocity potentials $\phi^{(i)} = \phi_0^{(i)} + \phi_{\mathrm{B}}^{(i)}$ and Eq. (45). Finally, Fig. 9d shows the resulting first- and second-order components of the displacement of the CFB. For better illustration, all quantities shown in Fig. 9 are scaled by the values $\eta_0 = 0.15\,\mathrm{m}$, $F_{1,0} = 4370\,\mathrm{N}$, $F_{3,0} = 1984\,\mathrm{N}$, and $\xi_0 = 0.19\,\mathrm{m}$. These values are chosen so that the respective scaled first-order quantities $\varepsilon\eta^{(1)}/\eta_0$, $\varepsilon F_1^{(1)}/F_{1,0}$, $\varepsilon F_3^{(1)}/F_{3,0}$, and $\varepsilon\xi^{(1)}/\xi_0$ have an amplitude of one for $t \to 50\,\mathrm{s}$.

Note that the CFB can only move in the vertical direction. Thus, the horizontal forces $\varepsilon F_1^{(1)}$ and $\varepsilon^2 F_1^{(2)}$ do not affect the motion of the CFB. Nevertheless, these forces are shown in Fig. 9 to investigate the loads that the CFB has to withstand in the open sea.

Considering Fig. 9a, it can be seen that the sea surface displacement $\varepsilon^2\eta_{\mathrm{inc}}^{(2)}$ oscillates in time with a higher oscillation frequency than $\varepsilon\eta_{\mathrm{inc}}^{(1)}$. Inserting the velocity potentials $\phi_0^{(1)}$ and $\phi_0^{(2)}$ from Eq. (25) into Eq. (A.2a), it is found that $\varepsilon\eta_{\mathrm{inc}}^{(1)}$ and $\varepsilon^2\eta_{\mathrm{inc}}^{(2)}$ oscillate in time with frequencies around ω_0 and $2\omega_0$, respectively.

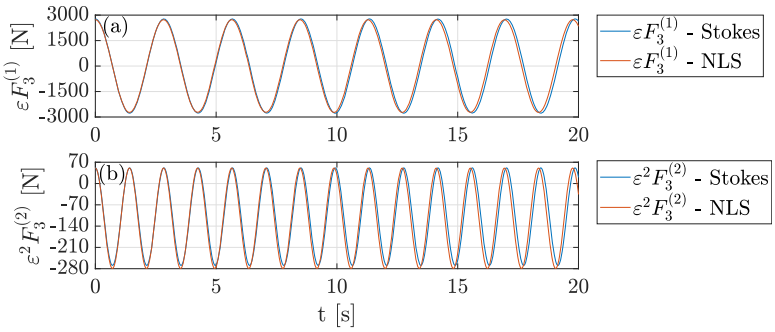

Fig. 8. (a) First- and (b) second-order component of the hydrodynamic force acting on the CFB in the vertical direction. The CFB is excited by Stokes waves and waves corresponding to the plane-wave solution of the NLS.

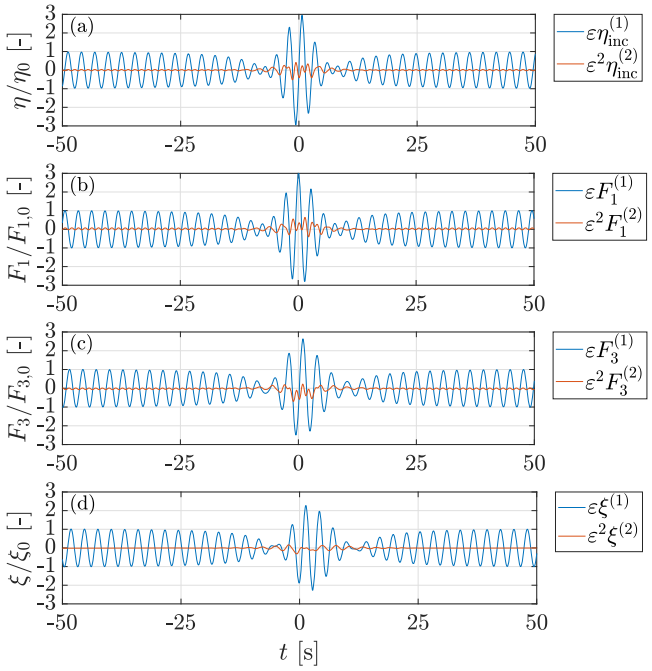

Fig. 9. FSI between the CFB and waves corresponding to the Peregrine breather solution of the NLS. It is shown the first- and second-order components of (a) the incoming water waves, the hydrodynamic forces acting in the (b) horizontal and (c) vertical direction, and (d) the displacement of the CFB.

In the following, the magnitudes of $\varepsilon\eta_{\mathrm{inc}}^{(1)}$ and $\varepsilon^2\eta_{\mathrm{inc}}^{(2)}$ are compared with each other by comparing their wave heights. Let $|\eta|_{\mathrm{H}}$ denote the time-dependent wave height of η. For some given timepoint t, $|\eta|_{\mathrm{H}}$ is defined as the difference between the next maximal and minimal value that η takes on around the timepoint t.

Outside the time period $[-30\,\mathrm{s}, 30\,\mathrm{s}]$, the sea surface displacements $\varepsilon\eta_{\mathrm{inc}}^{(1)}$ and $\varepsilon^2\eta_{\mathrm{inc}}^{(2)}$ behave regularly. Here, the quotient of their wave heights is about 3.7 %, i. e. $|\varepsilon^2\eta_{\mathrm{inc}}^{(2)}|_{\mathrm{H}}/|\varepsilon\eta_{\mathrm{inc}}^{(1)}|_{\mathrm{H}} = 3.7\,\%$. However, around $t = 0$, this quotient increases to $|\varepsilon^2\eta_{\mathrm{inc}}^{(2)}|_{\mathrm{H}}/|\varepsilon\eta_{\mathrm{inc}}^{(1)}|_{\mathrm{H}} = 14\,\%$. This means that the influence of the nonlinear second-order component $\varepsilon^2\eta_{\mathrm{inc}}^{(2)}$ on the total sea surface displacement $\eta_{\mathrm{inc}} = \varepsilon\eta_{\mathrm{inc}}^{(1)} + \varepsilon^2\eta_{\mathrm{inc}}^{(2)}$ increases significantly during the peak amplitude of the Peregrine breather solution around $t = 0$. This results directly from the fact that the wave envelope ψ of the Peregrine breather solution becomes higher and steeper around its peak amplitude.

The results for the sea surface displacements $\varepsilon\eta_{\mathrm{inc}}^{(1)}$ and $\varepsilon^2\eta_{\mathrm{inc}}^{(2)}$ can be directly transferred to the results for the acting hydrodynamic forces and the displacement of the CFB. Outside the time period $[-30\,\mathrm{s}, 30\,\mathrm{s}]$, Figs. 9b-9d show that the effect of the second-order components of the forces and displacement is small compared to the corresponding first-order results. However, during the developing of the peak amplitude of the Peregrine breather solution in the time period $[-30\,\mathrm{s}, 30\,\mathrm{s}]$, the effect of the corresponding second-order components becomes significant. It has to be noted that the second-order quantities $\varepsilon^2 F_1^{(2)}$ and $\varepsilon^2 F_3^{(2)}$ contain non-zero mean values, which represent drift forces. The appearance of drift forces in the nonlinear computation of the FSI is well-known in literature, see e.g. (Eatock Taylor and Hung, 1987). Therefore, it will not be discussed further here.

In Section 3.3.2, it is noted that the Peregrine breather solution of the NLS is conjectured in different studies to be a prototype of rogue ocean waves. Therefore, using the results presented in Fig. 9, it is shown that the FSI between a mechanical structure and a rogue wave can be simulated by using the Peregrine breather solution of the NLS, and that the second-order effects can significantly affect the corresponding overall FSI. As a result, these nonlinear effects appearing in the FSI should be considered, for example, when designing offshore structures that will operate in real ocean waves.

7.3. Irregular case: FSI with the perturbed Peregrine breather solution

Finally, results are presented for the FSI between the CFB and a random wave, which has been computed using the NLS. Here, the Peregrine breather solution is considered, which is initially perturbed by an irregular sea surface using the approach presented in Section 3.4. The wave envelope ψ of the perturbed Peregrine breather solution is computed using the ReSP scheme. To apply the ReSP scheme, an corresponding initial condition has to be determined. This initial condition is calculated considering the analytical Peregrine breather solution from Section 7.2 at time point $T = -20\,\mathrm{s}$, which is then perturbed using Eq. (24). Here, the perturbing sea surface displacement $\eta_{\mathrm{LC}}(x,t)$ is calculated using the Pierson-Moskowitz spectrum with peak frequency $\omega_{\mathrm{p}} = 0.25\,\frac{\mathrm{rad}}{\mathrm{s}}$ and significant wave height $H_{\mathrm{s}} = 1.5\,\mathrm{m}$. The temporal behavior of the amplitude $|\psi|$ of the perturbed Peregrine breather solution is presented in Fig. 10.

Fig. 10 shows that the characteristic localized peak of the unperturbed Peregrine breather solution shown in Fig. 2a can still be identified even when an initial perturbation is considered. However, fluctuations in the amplitude can be observed, which increase in time. At the end of the considered time domain, the fluctuations even become larger than the maximal peak amplitude of the corresponding unperturbed Peregrine breather solution, which has a height of $3\psi_0 = 4.5\,\mathrm{m}$. This indicates that an initial perturbation of the Peregrine breather solution considerably affects the corresponding wave dynamics over the whole time domain.

Next, the FSI is investigated, which occurs between the CFB and waves corresponding to the perturbed Peregrine breather solution presented in Fig. 10. All numerical results for the FSI are computed using the same spatial domain, time domain and discretizations as specified in Section 7.2. The corresponding results for the FSI are presented in

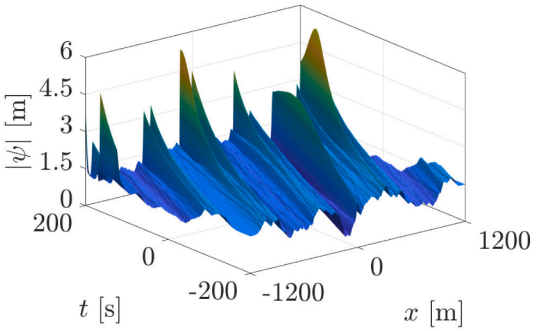

Fig. 10. Temporal behavior of the wave envelope of an initially perturbed Peregrine breather solution.

Fig. 11. Here, all results for the FSI are scaled by the same values η_0, $F_{1,0}$, $F_{3,0}$, and ξ_0 as have been used in Section 7.2 when presenting Fig. 9.

Compared to the results from Fig. 9, it can be seen that the initial perturbation of the Peregrine breather solution strongly affects the amplitude of the results for η, F_1, F_3, and ξ. However, their oscillation frequencies are not changed. This results from the fact that the considered initial perturbation only modifies the amplitude of the initial condition, but not their phase or frequency, see Eq. (24).

Similar to the results presented in Fig. 9, Fig. 11 shows that the second-order components of the forces and displacement become significant during the evolution of the peak amplitude of the Peregrine breather solution in the time interval $[-30\,\mathrm{s}, 30\,\mathrm{s}]$. However, in contrast to the results presented in Fig. 9, it is shown that these second-order components can contribute significantly to the FSI over the whole simulation time. It can be concluded that an initial perturbation can strongly affect the behavior of the Peregrine breather solution and the corresponding FSI with some mechanical structure.

Note that the Peregrine breather solution has been initially perturbed here using only realization of the irregular sea surface $\eta_{\mathrm{LC}}(x,t)$. Different realizations of $\eta_{\mathrm{LC}}(x,t)$ would lead to different temporal behaviors of the perturbed Peregrine breather solution and the FSI with the CFB. However, to make the scope of this work not too extensive, a stochastic analysis considering multiple realizations of $\eta_{\mathrm{LC}}(x,t)$ or varying ω_{p} and H_{s} is not presented here.

7.4. Discussion

It has been shown that the interaction between the CFB and the Peregrine breather solution of the NLS leads to large nonlinear second-order components in the acting hydrodynamic forces and the displacement of the CFB. On the other side, the Peregrine breather solution of the NLS is conjectured in different studies to be a prototype of rogue waves in the ocean, see e.g. (Dysthe and Trulsen, 1999; Shrira and Geogjaev, 2010; Dostal et al., 2020). Therefore, it has also been shown that nonlinear effects can contribute significantly to the corresponding FSI during rogue wave events. As a result, the computational method presented in this work can be used to estimate the linear and nonlinear hydrodynamic loads acting on mechanical structures during rogue wave events. These loads must be known to make, for example, mechanical structures resistant to rogue waves.

However, the proposed computational method also has limitations. First, the proposed approach using the NLS can only be used to compute the FSI in deep water. Second, the NLS can only be used to compute the FSI in water waves with a narrow spectral bandwidth. This remains true even if corresponding solutions of the NLS are initially perturbed by irregular sea surfaces. Considering Figs. 9a and 11a, it can be seen that the amplitude and phase of the incoming water waves change over time, but they oscillate in time with a nearly constant frequency. The same holds for the hydrodynamic forces acting on the CFB and the dynamics of the CFB, see Figs. 9b-9d and Figs. 11b-11d.

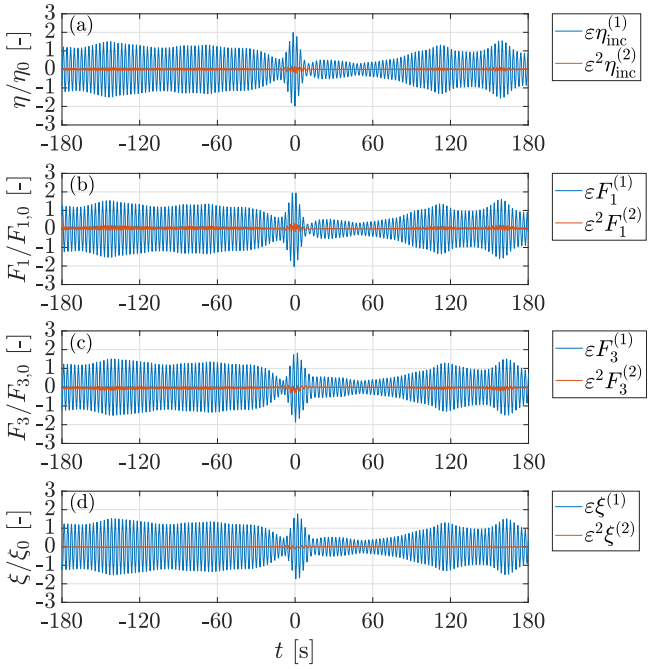

Fig. 11. FSI between the CFB and waves corresponding to the Peregrine breather solution of the NLS, which is initially perturbed by an irregular sea surface. It is shown the first- and second-order components of (a) the incoming water waves, the hydrodynamic forces acting in the (b) horizontal and (c) vertical direction, and (d) the displacement of the CFB.

To calculate the FSI in water waves with a broad spectral bandwidth, the random nonlinear Stokes waves introduced in Section 2.4 can be used. These waves are calculated by the sum of many regular waves depending on the underlying sea state, which does not have to be narrowbanded. However, as noted in Section 2.4, the computation of random nonlinear Stokes waves can be time-consuming due to the calculation of nonlinear wave-wave interactions. In comparison, when calculating water waves using the NLS, the calculation of nonlinear wave-wave interactions is not required, see Section 4. This can be also seen in the corresponding computation times. In further investigations, which are not shown here for brevity but can be found in (Hollm, 2025), the FSI between the CFB and nonlinear irregular Stokes waves has been considered. Here, the first-order sea surface displacement $\varepsilon\eta^{(1)}$ has been computed using Eq. (11) with $M = 120$ components. In this case, $M^2 = 14400$ nonlinear wave-wave interactions have to be considered to compute the nonlinear FSI with these waves. Under the same conditions (computation on a single computer; calculations performed in Matlab; no parallelization; same simulation time and computational domain), the irregular NLS results presented in Section 7.3 have been computed significantly faster by a factor of about ten when compared to the computation time of the FSI results in irregular Stokes waves. These investigations demonstrate that the NLS approach is significantly faster when computing the FSI for the considered scenarios. Therefore, it is found that NLS offers an interesting opportunity for many applications to efficiently investigate the behavior of structures excited by nonlinear ocean waves. For example, considering waves with a narrow spectral bandwidth, the NLS could be used to efficiently estimate whether nonlinear wave effects significantly affect the motion of the considered system and should be taken into account in further investigations. Furthermore, using, for example, the Peregrine breather solution of the NLS, it can be estimated with a low computational effort which hydrodynamic loads a fixed or free-floating structure have to withstand in rogue wave events. Therefore, using the computational method introduced in this work, it is shown that the usage of the NLS provides an efficient

way to compute the FSI. This establishes a novel pathway for research in this area.

Note that several extended versions of the NLS exist, which can model water waves with a larger wave steepness and broader spectral bandwidth than the NLS, or are not restricted to deep water. These extended versions can be found, for example, in (Mei, 1983; Dysthe, 1979; Trulsen and Dysthe, 1996; Toffoli et al., 2010; Adcock and Taylor, 2016). Based on the results presented in this work, it looks promising that these extended versions of NLS can be used to efficiently compute the FSI with water waves that are more general than those modeled by NLS. This should be studied in future studies.

8. Conclusion

This work presents a new method to compute the FSI in nonlinear water waves using the NLS. The application areas, accuracy, and computational effort of the presented method are analyzed. It is found that the FSI with waves corresponding to the NLS can be modeled up to an error of third-order in the wave steepness ε of the incoming water waves. Using the NLS, nonlinear wave effects of third order are directly considered in the FSI.

Comparing the waves corresponding to solutions of the NLS with random nonlinear Stokes waves, it is found that both can be used to compute the FSI between floating structures and nonlinear water waves. While Stokes waves can be used to investigate the motion of a floating structure in general broad-banded irregular nonlinear seas, the NLS can be used to simulate the motion of a floating structure in deep water waves with narrow spectral bandwidth and moderate wave steepness. Furthermore, the NLS can be used to investigate the FSI in rogue waves as different solutions of the NLS are conjectured to be prototypes of rogue waves. Moreover, in contrast to random nonlinear Stokes waves, nonlinear wave-wave interactions must not be considered when calculating nonlinear waves using the NLS. Therefore, the NLS offers an interesting possibility to efficiently investigate the temporal behavior of nonlinear water waves and the corresponding FSI with mechanical structures.

CRediT authorship contribution statement

Marten Hollm: Writing – original draft, Visualization, Validation, Software, Methodology, Investigation, Formal analysis, Conceptualization; **Robert Seifried:** Writing – review & editing, Supervision, Methodology, Funding acquisition.

Declaration of competing interest

The authors declare that they have no known competing financial interests or personal relationships that could have appeared to influence the work reported in this paper.

Acknowledgements

The authors would like to thank the German Research Foundation (DFG) for the financial support of the project 528383251.

Appendix A. Computation of the sea surface displacement

When integrating the hydrodynamic pressure p over the wetted surface of the mechanical structure, it has to be noted that the wetted surface changes with the sea surface displacement η. Therefore, it is briefly described how the sea surface displacement η corresponding to a given velocity potential ϕ can be computed.

Similar to the derivation of Eq. (3), the sea surface displacement η can be expressed by a sequence of expressions that differ in their order of approximation. Applying the Taylor series expansion around $z=0$ on Eq. (1c) and considering all terms up to order $\mathcal{O}(\phi^4)$, the sea surface displacement η is given by

$$\eta = \left[-\frac{1}{g}\left(\phi_t + \frac{1}{2}\nabla\phi\cdot\nabla\phi\right) + \frac{1}{g^2}\left(\phi_t\phi_{tz} + \frac{1}{2}\frac{\partial}{\partial z}\left(\phi_t\,\nabla\phi\cdot\nabla\phi\right)\right) - \frac{1}{2g^3}\frac{\partial}{\partial z}\left(\left(\phi_t\right)^2\phi_{tz}\right)\right]_{z=0} + \mathcal{O}(\phi^4). \tag{A.1}$$

Given the velocity potentials $\phi^{(1)}$, $\phi^{(2)}$, and $\phi^{(3)}$, expressions for the first three components $\eta^{(1)}$, $\eta^{(2)}$ and $\eta^{(3)}$ of the sea surface displacement η can be derived by substituting the expansions from Eq. (4) into Eq. (A.1). The first two sea surface displacements $\eta^{(1)}$ and $\eta^{(2)}$ are given by

$$\eta^{(1)} = \left[-\frac{1}{g}\phi_t^{(1)}\right]_{z=0}, \tag{A.2a}$$

$$\eta^{(2)} = \left[-\frac{1}{g}\left(\phi_t^{(2)} + \frac{1}{2}\nabla\phi^{(1)}\cdot\nabla\phi^{(1)}\right) + \frac{1}{g^2}\left(\phi_t^{(1)}\phi_{tz}^{(1)}\right)\right]_{z=0}, \tag{A.2b}$$

see e.g. (Eatock Taylor and Hung, 1987). As $\eta^{(3)}$ is not needed in this work, the corresponding formula for $\eta^{(3)}$ is not stated here.

Appendix B. Computation of the velocity potentials corresponding to the NLS

In Section 3.2, the derivation of the NLS is sketched. Here, PDEs and BCs at $Z=0$ have to be solved to compute the unknowns A_{ij} and $\bar{\phi}_i$, which appear in Eq. (19) up to the order $\mathcal{O}(\varepsilon^3)$. The corresponding PDEs and BCs at $Z=0$ are given by

$$\begin{cases} A_{10,Z} + \mathrm{i}A_{10,X} = 0, & \text{for } Z<0,\\ A_{10} = -\frac{\mathrm{i}\omega_0}{k_0}B, & \text{for } Z=0, \end{cases} \tag{B.1a}$$

$$\begin{cases} A_{20,Z} + \mathrm{i}A_{20,X} = 0, & \text{for } Z<0,\\ A_{20} = 0, & \text{for } Z=0, \end{cases} \tag{B.1b}$$

$$\begin{cases} A_{11,Z} + \mathrm{i}A_{11,X} = -\frac{1}{2k_0}\left(A_{10,XX} + A_{10,ZZ}\right), & \text{for } Z<0,\\ A_{11} = \frac{\omega_0}{2k_0^2}B_X, & \text{for } Z=0, \end{cases} \tag{B.1c}$$

$$\begin{cases} A_{30,Z} + \mathrm{i}A_{30,X} = 0, & \text{for } Z<0,\\ A_{30} = 0, & \text{for } Z=0, \end{cases} \tag{B.1d}$$

$$\begin{cases} A_{21,Z} + \mathrm{i}A_{21,X} = -\frac{1}{4k_0}\left(A_{20,XX} + A_{20,ZZ}\right), & \text{for } Z<0,\\ A_{21} = 0, & \text{for } Z=0, \end{cases} \tag{B.1e}$$

$$\begin{cases} A_{12,Z} + \mathrm{i}A_{12,X} = -\frac{1}{2k_0}\left(A_{11,XX} + A_{11,ZZ}\right), & \text{for } Z<0,\\ A_{12} = \frac{1}{2}\mathrm{i}k_0\omega_0|B|^2B + \frac{3\mathrm{i}\omega_0}{8k_0^3}B_{XX}, & \text{for } Z=0, \end{cases} \tag{B.1f}$$

$$\begin{cases} \bar{\phi}_{0,XX} + \bar{\phi}_{0,ZZ} + \bar{\phi}^*_{0,XX} + \bar{\phi}^*_{0,ZZ} = 0, & \text{for } Z<0,\\ \bar{\phi}_{0,Z} + \bar{\phi}^*_{0,Z} = 2\omega_0\left(|B|^2\right)_X, & \text{for } Z=0. \end{cases} \tag{B.1g}$$

Noted that in addition to the functions appearing in Eq. (B.1a), the mean velocity potential $\bar{\phi}_1$ also appears in Eq. (19) with order $\mathcal{O}(\varepsilon^3)$. However, as is shown in Section 4, the mean velocity potential $\bar{\phi}_1$ is not needed to formulate the FSI method used in this work. Therefore, corresponding equations to compute $\bar{\phi}_1$ are not stated here.

When solving Eq. (B.1a), the functions A_{ij}, which appear in Eq. (18a) up to the order $\mathcal{O}(\varepsilon^3)$, are given in terms of B by

$$A_{10} = -\frac{\mathrm{i}\omega_0}{k_0}\widetilde{B},\quad A_{11} = \frac{\omega_0}{2k_0}\widetilde{B}_X,\quad A_{12} = \frac{1}{16}\mathrm{i}k_0\omega_0\widetilde{C} + \frac{3\mathrm{i}\omega_0}{8k_0^3}\widetilde{B}_{XX},\quad A_{20} = 0,\quad A_{21} = 0,\quad A_{30} = 0, \tag{B.2}$$

with $\widetilde{B}(X,Z,T) = B(X-\mathrm{i}Z,T)$, $C(X,T) = 8|B(X,T)|^2B(X,T)$, and $\widetilde{C}(X,Z,T) = C(X-\mathrm{i}Z,T)$.

Furthermore, the functions B_{ij} and $\bar{\eta}_0 + \bar{\eta}_0^*$, which appear in Eq. (18b) up to the order $\mathcal{O}(\varepsilon^3)$, are given in terms of B and $\bar{\phi}_0$ by

$$B_{20} = k_0 B^2, \quad B_{30} = \frac{3}{2} k_0^2 B^3, \quad B_{21} = -\mathrm{i} k_0 B B_X, \\ \bar{\eta}_0 + \bar{\eta}_0^* = -\frac{1}{g}\left(\bar{\phi}_0 + \bar{\phi}_0^*\right)_T, \quad \text{for } Z = 0. \tag{B.3}$$

At this point, the mean velocity potential $\bar{\phi}_0$ and the mean surface displacement $\bar{\eta}_0$ must still be determined in terms of B. To compute $\bar{\phi}_0$, Eq. (B.1g) has to be solved. This is done using the Fourier transform $\mathcal{F}$ and its inverse $\mathcal{F}^{-1}$. In addition, the solution approach presented in (Lo and Mei, 1985) is followed. Applying the Fourier transform with respect to the coordinate X on Eq. (B.1g) and using $\mathcal{F}\left(\bar{\phi}_{0,X}\right) = \mathrm{i} k \mathcal{F}\left(\bar{\phi}_0\right)$, the mean velocity potential $\bar{\phi}_0$ can be calculated to be

$$\bar{\phi}_0(X, Z, T) + \bar{\phi}_0^*(X, Z, T) = \mathcal{F}^{-1}\left(2\mathrm{i}\omega_0 \operatorname{sgn}(k) \mathcal{F}\left(|B|^2\right) \mathrm{e}^{|k|Z}\right). \tag{B.4}$$

Having computed $\bar{\phi}_0$, the mean sea surface displacement $\bar{\eta}_0$ is given by

$$\bar{\eta}_0 + \bar{\eta}_0^* = -\frac{1}{g}\left[\left(\bar{\phi}_0 + \bar{\phi}_0^*\right)_T\right]_{Z=0} = \frac{2\omega_0}{g} \frac{\partial}{\partial T}\left(\mathcal{H}\left(|B|^2\right)\right). \tag{B.5}$$

Here, $\mathcal{H}$ denotes the Hilbert transform.

Appendix C. Numerical computation of ϕ_B

In the following a finite difference scheme is presented, which is used to discretize Eq. (41) and to compute the Fourier coefficients $\hat{\phi}_{\mathrm{B},m}^{(i)}$ of the body disturbance velocity potential ϕ_B. Here, only one index $m \in \{-\frac{N_F}{2}, \ldots, \frac{N_F}{2} - 1\}$ and $i \in \{1, 2\}$ is considered. In order to simplify the notation for readability, the indices m, (i) and B are omitted in the following, i. e. $\hat{\phi}_{\mathrm{B},m}^{(i)}$ becomes simply $\hat{\phi}$.

For some numbers $N, M, P \in \mathbb{N}$ and some time $T \in \mathbb{R}_+$, the solution $\hat{\phi}$ is computed on the (r, z, t)-grid with the grid points

$$0 < r_1 < r_2 < \ldots < r_{N+1} = R_\Omega, \\ 0 = z_1 > z_2 > \ldots > z_{M+1} = -h, \\ 0 = t^1 < t^2 < \ldots < t^{P+1} = T. \tag{C.1}$$

For $i = 1, \ldots, N+1$, $j = 1, \ldots, M+1$ and $p = 1, \ldots, P+1$, the grid points are defined as

$$r_i := (i - \frac{1}{2})\Delta r, \quad z_j := -(j-1)\Delta z, \quad t^p := (p-1)\Delta t, \tag{C.2}$$

with

$$\Delta r := \frac{R_\Omega}{N + 1/2}, \quad \Delta z := \frac{h}{M}, \quad \Delta t := \frac{T}{P}. \tag{C.3}$$

The numerical approximation of $\hat{\phi}$ at the space point (r_i, z_j) and time point t^p is defined by $\hat{\phi}_{i,j}^p$, i. e. $\hat{\phi}_{i,j}^p \approx \hat{\phi}(r_i, z_j, t^p)$. In the following, the unknown $\hat{\phi}_{i,j}^p$ are computed by discretizing Eq. (41) using a finite difference method with a second-order accuracy in time and space. Note that some of the $(N+1)(M+1)$ space points from Eq. (C.1) are located in $\bar{C}_2$. Most unknowns $\hat{\phi}_{i,j}^p$ inside the CFB are set to zero. However, interior grid points (r_i, z_j) in $\bar{C}_2$ with at least one horizontal or vertical neighbor in $\mathring{\Omega}_2$, so-called ghost points, must be treated separately. These points are needed to compute the unknowns $\hat{\phi}_{i,j}^p$, which have a neighbor in $\bar{C}_2$

C.1. Laplace equation inside the fluid

Inside the fluid, the Laplace Eq. (41a) holds. This equation is discretized applying a central finite difference approximation of second order. At the grid point $(r_i, z_j) \in \mathring{\Omega}_2$ and timpoint t^p, the corresponding approximation of Eq. (41a) reads

$$\frac{\hat{\phi}_{i+1,j}^p - 2\hat{\phi}_{i,j}^p + \hat{\phi}_{i-1,j}^p}{\Delta r^2} + \frac{1}{r_i}\frac{\hat{\phi}_{i+1,j}^p - \hat{\phi}_{i-1,j}^p}{2\Delta r} \\ - \frac{m^2}{r_i^2}\hat{\phi}_{i,j}^p + \frac{\hat{\phi}_{i,j+1}^p - 2\hat{\phi}_{i,j}^p + \hat{\phi}_{i,j-1}^p}{\Delta z^2} = 0. \tag{C.4}$$

Note that for $i = 1$, the grid points $(r_i, z_j) \in \mathring{\Omega}_2$ do not have a neighbor in the negative r-direction. However, for $i = 1$, the sum of all terms depending on $\hat{\phi}_{i-1,j}^p$ simplify to zero. Therefore, the values of $\hat{\phi}_{i-1,j}^p$ are not needed for $i = 1$, and the approximation from Eq. (C.4) can also be applied for $i = 1$.

C.2. Boundary conditions at the outer boundary and bottom of the sea

The BCs at the bottom of the sea and the outer boundary are given by Eqs. (41c) and (41e), respectively. Respective second-order approximations are given by

$$\frac{\hat{\phi}_{N-1,j} - 4\hat{\phi}_{N,j} + 3\hat{\phi}_{N+1,j}}{2\Delta r} = 0, \quad \text{for } j = 1, \ldots, M+1, \tag{C.5}$$

$$\frac{\hat{\phi}_{i,M-1} - 4\hat{\phi}_{i,M} + 3\hat{\phi}_{i,M+1}}{2\Delta z} = 0, \quad \text{for } i = 1, \ldots, N+1. \tag{C.6}$$

Note that both Eqs. (C.5) and (C.6) can be applied at the corner point (r_{N+1}, z_{M+1}), having two equations to compute the unknown $\hat{\phi}_{N+1,M+1}$. In this work, the sum of those two equations is used as a single equation to calculate $\hat{\phi}_{N+1,M+1}$. This approach is consistently applied at each corner point of $\mathring{\Omega}_2$ where two equations can determine one value $\hat{\phi}_{i,j}$.

C.3. Boundary condition at the sea surface

The BC at the sea surface is given by Eq. (41d). An implicit discretization of Eq. (41d), which is accurate up to second order in time and space, is given by

$$\frac{\hat{\phi}_{i,1}^{p+1} - 2\hat{\phi}_{i,1}^p + \hat{\phi}_{i,1}^{p-1}}{\Delta t^2} + \frac{g}{4}\left\{\frac{3\hat{\phi}_{i,1}^{p+1} - 4\hat{\phi}_{i,2}^{p+1} + \hat{\phi}_{i,3}^{p+1}}{2\Delta z} + 2\frac{3\hat{\phi}_{i,1}^{p} - 4\hat{\phi}_{i,2}^{p} + \hat{\phi}_{i,3}^{p}}{2\Delta z} \right. \\ \left. + \frac{3\hat{\phi}_{i,1}^{p-1} - 4\hat{\phi}_{i,2}^{p-1} + \hat{\phi}_{i,3}^{p-1}}{2\Delta z}\right\} + 2\mu_i \frac{\hat{\phi}_{i,1}^{p+1} - \hat{\phi}_{i,1}^{p-1}}{2\Delta t} + \mu_i^2 \frac{\hat{\phi}_{i,1}^{p+1} + 2\hat{\phi}_{i,1}^{p} + \hat{\phi}_{i,1}^{p-1}}{4} \\ = \hat{G}(r_i, z_1, t^p), \quad \text{for all } i \text{ with } R \le r_i \le R_\Omega. \tag{C.7}$$

whereby $\mu_i := \mu(r_i)$.

C.4. Boundary condition at the surface of the cylindrical floating body

The BC at the surface $\partial\bar{C}_2$ of the CFB is given by Eq. (41b). In general, the boundary $\partial\bar{C}_2$ is not located at the grid given in Eq. (C.1). Instead, Eq. (41b) is used to derive equations that can be used to compute the unknown $\hat{\phi}$ at the ghost points inside the CFB.

For some ghost point $\mathbf{g} \in \bar{C}_2$, let $\mathbf{p}$ be the nearest point to $\mathbf{g}$ on $\partial\bar{C}_2$. Since $\mathbf{p} \in \partial\bar{C}_2$, the BC (41b) also holds at $\mathbf{p}$. Therefore, an approximation of the term $\hat{\phi}_r n^r + \hat{\phi}_z n^z$ at $\mathbf{p}$ has to be found using the value of $\hat{\phi}$ at the ghost point $\mathbf{g}$ and other grid points neighbored to $\mathbf{p}$.

Let $\mathcal{I}$ be the set of all indices of all grid points, which are used to approximate the value of $\hat{\phi}_r n^r + \hat{\phi}_z n^z$ at $\mathbf{p}$. Furthermore, let $\mathbf{q}_I \in \mathbb{R}^2$ denote the grid point corresponding to the index $I \in \mathcal{I}$. An approximation of $\hat{\phi}_r n^r + \hat{\phi}_z n^z$ at p of second order in space is searched of the form

$$\hat{\phi}_r(\mathbf{p}, t^p) n^r + \hat{\phi}_z(\mathbf{p}, t^p) n^z \approx \sum_{I \in \mathcal{I}} h_I \hat{\phi}(\mathbf{q}_I, t^p). \tag{C.8}$$

To compute the values of the coefficients h_I, $I \in \mathcal{I}$, a Taylor series expansion of $\hat{\phi}(\mathbf{q}_I, t^p)$ around $\mathbf{p}$ is considered and substituted into Eq. (C.8).

Let $\hat{\phi}_I^p$ be the finite difference approximation of $\hat{\phi}$ evaluated at $(\mathbf{q}_I, t^p)$, i. e. $\hat{\phi}_I^p \approx \hat{\phi}(\mathbf{q}_I, t^p)$. Having computed the values of h_I, an approximation of the BC (41b) of second order is given by

$$\sum_{I \in \mathcal{I}} h_I \hat{\phi}_I^p = -\hat{\phi}_{0,r}(\mathbf{p}, t^p) n^r - \hat{\phi}_{0,z}(\mathbf{p}, t^p) n^z + u_3 n^z \hat{1} + \hat{V}. \tag{C.9}$$

References

Adcock, T. A.A., Taylor, P.H., 2016. Non-linear evolution of uni-directional focussed wave-groups on a deep water: A comparison of models. Appl. Ocean Res. 59, 147–152. https://doi.org/10.1016/j.apor.2016.05.012

Antoine, X., Duboscq, R., 2015. GPELab, a Matlab toolbox to solve Gross-Pitaevskii equations II: Dynamics and stochastic simulations. Comput. Phys. Commun. 193, 95–117. https://doi.org/10.1016/j.cpc.2015.03.012

Bai, W., Teng, B., 2013. Simulation of second-order wave interaction with fixed and floating structures in time domain. Ocean Eng. 74, 168–177. https://doi.org/10.1016/j.oceaneng.2013.07.014

Büchmann, B., Skourup, J., Cheung, K.F., 1998. Run-up on a structure due to second-order waves and a current in a numerical wave tank. Appl. Ocean Res. 20 (5), 297–308. https://doi.org/10.1016/S0141-1187(98)00022-4

Carter, J.D., Curtis, C.W., Kalisch, H., 2020. Particle trajectories in nonlinear Schrödinger models. Water Waves 2, 31–57. https://doi.org/10.1007/s42286-019-00008-7

Chabchoub, A., 2013. An experimental study on breathers in water waves. Ph.D. thesis, Hamburg University of Technology.

Chabchoub, A., Akhmediev, N., Hoffmann, N.P., 2012. Experimental study of spatiotemporally localized surface gravity water waves. Phys. Rev. E 86 (1), 016311. https://doi.org/10.1103/PhysRevE.86.016311

Clauss, G., Lehmann, E., Östergaard, C., 1988. Meerestechnische Konstruktionen. Berlin, Heidelberg: Springer. 1 edition.

Dostal, L., Hollm, M., Kreuzer, E., 2020. Study on the behavior of weakly nonlinear water waves in the presence of random wind forcing. Nonlinear Dyn. 99 (3), 2319–2338. https://doi.org/10.1007/s11071-019-05416-5

Dysthe, K.B., 1979. Note on a modification to the nonlinear Schrödinger equation for application to deep water waves. Proc. R. Soc. A: Math. Phys. Eng. Sci. 369, 105–114. https://doi.org/10.1098/rspa.1979.0154

Dysthe, K.B., Trulsen, K., 1999. Note on breather type solutions of the NLS as models for freak-waves. Phys. Scr. T82, 48–52. https://doi.org/10.1238/Physica.Topical.082a00048

Eatock Taylor, R., Hung, S.M., 1987. Second order diffraction forces on a vertical cylinder in regular waves. Appl. Ocean Res. 9 (1), 19–30. https://doi.org/10.1016/0141-1187(87)90028-9

Garrett, C.J.R., 1971. Wave forces on a circular dock. J. Fluid Mech. 46 (1), 129–139. https://doi.org/10.1017/S0022112071000430

Greaves, D., Iglesias, G., 2018. Wave and tidal energy. Hoboken, NY: John Wiley & Sons. https://doi.org/10.1002/9781119014492

Hollm, M., 2025. A new Computational Method for the Fluid-structure Interaction in Random Nonlinear Ocean Waves. Ph.D. thesis, Hamburg University of Technology. https://doi.org/10.15480/882.14990

Hollm, M., Dostal, L., Carter, J.D., Seifried, R., 2024. Determination of particle paths and hydrodynamic forces of random wind forced nonlinear ocean waves. Proc. Inst. Mech. Eng., Part M: J. Eng. Maritime Environ. 238 (2), 406–416. https://doi.org/10.1177/14750902231196812

Hollm, M., Dostal, L., Fischer, H., Seifried, R., 2021. Study on the interaction of nonlinear water waves considering random seas. Proc. Appl. Math. Mech. 20 (1), e202000307. https://doi.org/10.1002/pamm.202000307

Hollm, M., Dostal, L., Seifried, R., 2022a. Hydrodynamic forces acting on cylindrical piles subjected to wind-forced random nonlinear water waves. In: Lacarbonara, W., Balachandran, B., Leamy, M.J., Ma, J., Tenreiro Machado, J.A., Stepan, G. (Eds.), Advances in Nonlinear Dynamics. Springer International Publishing, Cham, pp. 95–105. https://doi.org/10.1007/978-3-030-81162-4

Hollm, M., Dostal, L., Yurchenko, D., Seifried, R., 2022b. Performance increase of wave energy harvesting of a guided point absorber. Eur. Phys. J. Spec. Topic. 231 (8), 1465–1473. https://doi.org/10.1140/epjs/s11734-022-00497-7

Hollm, M., Seifried, R., 2023. Hydrodynamic forces acting on mechanical systems in linear and nonlinear ocean waves. Proc. Appl. Math. Mech. 23 (2), e202300141. https://doi.org/10.1002/pamm.202300141

Kinoshita, T., Bao, W., 2000. Third-order wave diffraction by a truncated circular cylinder. Proc. Inst. Mech. Eng., Part C: J. Mech. Eng. Sci. 214 (6), 789–800. https://doi.org/10.1243/0954406001523786

Lin, P., 2008. Numerical modeling of water waves. London, New York: Taylor & Francis. https://doi.org/10.1201/9781482265910

Lo, E., Mei, C.C., 1985. A numerical study of water-wave modulation based on a higher-order nonlinear Schrödinger equation. J. Fluid Mech. 150, 395–416. https://doi.org/10.1017/S0022112085000180

Ma, Q.W., Yan, S., 2006. Quasi ALE finite element method for nonlinear water waves. J. Comput. Phys. 212 (1), 52–72. https://doi.org/10.1016/j.jcp.2005.06.014

Malenica, Š., Molin, B., 1995. Third-harmonic wave diffraction by a vertical cylinder. J. Fluid Mech. 302, 203–229. https://doi.org/10.1017/S0022112095004071

Mei, C.C., 1983. The applied dynamics of ocean surface waves. New York: John Wiley & Sons.

Mitsuyasu, H., Tasai, F., Suhara, T., Mizuno, S., Okhuso, M., Honda, T., Rikiishi, K., 1975. Observation of the directional spectrum of ocean waves using a cloverleaf buoy. J. Phys. Oceanogr. 5 (4), 750–760. https://doi.org/10.1175/1520-0485(1975)005<0750:OOTDSO>2.0.CO;2

Newman, J.N., 2018. Marine hydrodynamics. Cambridge: The MIT press.

Ogilvie, T.F., 1983. Second-order hydrodynamic effects on ocean platforms. In: Yeung, R.W. (Ed.), Proceedings of the International Workshop on Ship and Platform Motions, University of California, Berkeley, pp. 205–265.

Onorato, M., Osborne, A.R., Serio, M., Bertone, S., 2001. Freak waves in random oceanic sea states. Phys. Rev. Lett. 86 (25), 5831–5834. https://doi.org/10.1103/PhysRevLett.86.5831

Osborne, A.R., 2010. Nonlinear Ocean Waves and the Inverse Scattering Transform. Amsterdam: Academic Press. 1 edition.

Peregrine, D.H., 1983. Water waves, nonlinear Schrödinger equations and their solutions. J. Austral. Math. Soc. Ser. B Appl. Math. 25 (1), 16–43. https://doi.org/10.1017/S0334270000003891

Rahman, M., Bora, S.N., Satish, M.G., 1999. A note on second-order wave forces on a circular cylinder in finite water depth. Appl. Math. Lett. 12 (1), 63–70. https://doi.org/10.1016/S0893-9659(98)00128-1

Shao, Y., Zheng, Z., Liang, H., Chen, J., 2022. A consistent second-order hydrodynamic model in the time domain for floating structures with large horizontal motions. Comput.-Aided Civ. Infrastruct. Eng. 37 (7), 894–914. https://doi.org/10.1111/mice.12782

Shao, Y.-L., Faltinsen, O.M., 2013. Second-order diffraction and radiation of a floating body with small forward speed. J. Offshore Mech. Arct. Eng. 135 (1), 011301. https://doi.org/10.1115/1.4006929

Sharma, J.N., Dean, R.G., 1979. Development and Evaluation of a Procedure for Simulating a Random Directional Second-Order Sea Surface and Associated Wave Forces. Ocean Engineering Report 20, University of Delaware, Newark.

Shemer, L., Dorfman, B., 2008. Experimental and numerical study of spatial and temporal evolution of nonlinear wave groups. Nonlinear Process. Geophys. 15 (6), 931–942. https://doi.org/10.5194/npg-15-931-2008

Shrira, V.I., Geogjaev, V.V., 2010. What makes the Peregrine soliton so special as a prototype of freak waves? J. Eng. Math. 67, 11–22. https://doi.org/10.1007/s10665-009-9347-2

Skourup, J., Cheung, K.F., Bingham, H.B., Büchmann, B., 2000. Loads on a 3D body due to second-order waves and a current. Ocean Eng. 27 (7), 707–727. https://doi.org/10.1016/S0029-8018(99)00013-X

Slunyaev, A., Clauss, G.F., Klein, M., Onorato, M., 2013. Simulations and experiments of short intense envelope solitons of surface water waves. Phys. Fluid. 25 (6), 067105. https://doi.org/10.1063/1.4811493

Slunyaev, A., Pelinovsky, E., Guedes Soares, C., 2014. Reconstruction of extreme events through numerical simulations. J. Offshore Mech. Arct. Eng. 136 (1), 011302. https://doi.org/10.1115/1.4025545

Stokes, G.G., 1847. On the theory of oscillatory waves. Trans. Cambridge Philos. Soc. 8, 441–455.

Toffoli, A., Gramstad, O., Trulsen, K., Monbaliu, J., Bitner-Gregersen, E., Onorato, M., 2010. Evolution of weakly nonlinear random directional waves: laboratory experiments and numerical simulations. J. Fluid Mech. 664, 313–336. https://doi.org/10.1017/S002211201000385X

Trulsen, K., Dysthe, K.B., 1996. A modified nonlinear Schrödinger equation for broader bandwidth gravity waves on deep water. Wave Motion 24 (3), 281–289. https://doi.org/10.1016/S0165-2125(96)00020-0

Witt, A., 2019. Inducing predefined nonlinear rogue waves on basis of breather solutions. Ph.D. thesis, Hamburg University of Technology. https://doi.org/10.15480/882.2224

Yeung, R.W., 1981. Added mass and damping of a vertical cylinder in finite-depth waters. Appl. Ocean Res. 3 (3), 119–133. https://doi.org/10.1016/0141-1187(81)90101-2

Yeung, R.W., Peiffer, A., Tom, N., Matlak, T., 2012. Design, analysis, and evaluation of the UC-Berkeley wave-energy extractor. J. Offshore Mech. Arct. Eng. 134 (2), 021902. https://doi.org/10.1115/1.4004518